Probing Kilonova Ejecta Properties Using a Catalog of Short Gamma-Ray Burst Observations

J. C. Rastinejad[1], W. Fong[1], C. D. Kilpatrick[1], K. Paterson[1], N. R. Tanvir[2], A. J. Levan[3,4], B. D. Metzger[5,6], E. Berger[7], R. Chornock[1], B. E. Cobb[8], T. Laskar[9], P. Milne[10], A. E. Nugent[1], and N. Smith[10]

[1] Center for Interdisciplinary Exploration and Research in Astrophysics and Department of Physics and Astronomy, Northwestern University, 2145 Sheridan Road, Evanston, IL 60208-3112, USA; jillianrastinejad2024@u.northwestern.edu
[2] School of Physics and Astronomy, University of Leicester, University Road, Leicester, LE1 7RH, UK
[3] Department of Astrophysics/IMAPP, Radboud University, 6525 AJ Nijmegen, The Netherlands
[4] Department of Physics, University of Warwick, Coventry, CV4 7AL, UK
[5] Center for Computational Astrophysics, Flatiron Institute, 162 W. 5th Avenue, New York, NY 10011, USA
[6] Department of Physics and Columbia Astrophysics Laboratory, Columbia University, New York, NY 10027, USA
[7] Center for Astrophysics|Harvard & Smithsonian, 60 Garden St. Cambridge, MA 02138, USA
[8] Department of Physics, The George Washington University, Washington, DC 20052, USA
[9] Department of Physics, University of Bath, Claverton Down, Bath, BA2 7AY, UK
[10] Steward Observatory, University of Arizona, 933 North Cherry Avenue, Tucson, AZ 85721-0065, USA

Received 2021 January 11; revised 2021 May 17; accepted 2021 May 21; published 2021 August 2

Abstract

The discovery of GW170817 and GRB 170817A in tandem with AT 2017gfo cemented the connection between neutron star mergers, short gamma-ray bursts (GRBs), and kilonovae. To investigate short GRB observations in the context of diverse kilonova behavior, we present a comprehensive optical and near-IR catalog of 85 bursts discovered over 2005–2020 on timescales of $\lesssim 12$ days. The sample includes previously unpublished observations of 23 bursts and encompasses both detections and deep upper limits. We identify 11.8% and 15.3% of short GRBs in our catalog with upper limits that probe luminosities lower than those of AT 2017gfo and a fiducial neutron star–black hole kilonova model (for pole-on orientations), respectively. We quantify the ejecta masses allowed by the deepest limits in our catalog, constraining blue and "extremely blue" kilonova components of 14.1% of bursts to $M_{\rm ej} \lesssim 0.01$–$0.1~M_{\odot}$. The sample of short GRBs is not particularly constraining for red kilonova components. Motivated by the large catalog, as well as model predictions of diverse kilonova behavior, we investigate modified search strategies for future follow-up to short GRBs. We find that ground-based optical and near-IR observations on timescales of $\gtrsim 2$ days can play a significant role in constraining more diverse outcomes. We expect future short GRB follow-up efforts, such as from the James Webb Space Telescope, to expand the reach of kilonova detectability to redshifts of $z \approx 1$.

Unified Astronomy Thesaurus concepts: Gamma-ray bursts (629); Neutron stars (1108)

Supporting material: machine-readable table

1. Introduction

The detection of the binary neutron star (BNS) merger GW170817 began a new era of multimessenger astronomy by providing the first direct link between gravitational wave (GW) detected compact object mergers and multiband electromagnetic transients (Abbott et al. 2017a, 2017c). The nearly simultaneous gamma-ray burst (GRB) GRB 170817A (Abbott et al. 2017b; Goldstein et al. 2017; Savchenko et al. 2017) linked BNS mergers to short GRBs, cosmological transients with durations $\lesssim 2$ s, and harder gamma-ray spectra (Norris et al. 1984; Kouveliotou et al. 1993). Short GRBs are accompanied by a broadband afterglow originating in a jet launched from the merger remnant (Sari et al. 1998; Berger 2014). At early times, the optical light curves of short GRBs are dominated by this rapidly fading, nonthermal afterglow. The ensuing optical and near-IR (NIR) counterpart to GRB 170817 and GW170817, AT 2017gfo, also connected BNS mergers with kilonovae (Arcavi et al. 2017; Chornock et al. 2017; Coulter et al. 2017; Cowperthwaite et al. 2017; Díaz et al. 2017; Drout et al. 2017; Fong et al. 2017; Gall et al. 2017; Hu et al. 2017; Kasliwal et al. 2017a; Lipunov et al. 2017; McCully et al. 2017; Nicholl et al. 2017; Pian et al. 2017; Shappee et al. 2017; Smartt et al. 2017; Soares-Santos et al. 2017; Tanvir et al. 2017; Utsumi et al. 2017; Valenti et al. 2017; Villar et al.

2017; Pozanenko et al. 2018), thermal transients powered by the radioactive decay of r-process elements synthesized in neutron-rich ejecta (Li & Paczyński 1998; Metzger et al. 2010; Barnes & Kasen 2013; Rosswog et al. 2014). As the only well-localized GW merger in the local ($z < 0.05$) universe, this event allowed for extremely well sampled, multiband light curves of the kilonova counterpart, enabling us to directly compare AT 2017gfo to observations of its cosmological analogs.

In addition to BNS mergers, some neutron star–black hole (NSBH) mergers are predicted to produce kilonovae. Thus far, there are only a few potential detections of an NSBH merger, including GW190426_152155 (Abbott et al. 2021) and GW190814 (Abbott et al. 2020b), though none have a confirmed associated kilonova to date (e.g., Gomez et al. 2019; Hosseinzadeh et al. 2019; Ackley et al. 2020; Anand et al. 2021; Andreoni et al. 2020; Gompertz et al. 2020a; Morgan et al. 2020; Paterson et al. 2021; Vieira et al. 2020). The lack of electromagnetic (EM) emission from GW190814 is consistent with the finding that the primary black hole (BH) mass is $23~M_{\odot}$, as a high-mass BH would not disrupt the NS until it is inside the BH's innermost stable circular orbit, thus accreting all of the ejecta (Foucart et al. 2013; Fernández & Metzger 2016). Kilonovae from BNS and NSBH systems are of particular interest in GW follow-up, as they radiate emission relatively isotropically (Li & Paczyński 1998;

Metzger et al. 2010), unlike other signatures of these mergers (e.g., jetted afterglows), which are generally detected at pole-on orientations.

Theoretical studies have long predicted a diversity of observed kilonova behavior (Li & Paczyński 1998; Metzger & Fernández 2014; Kawaguchi et al. 2020a). Model light curves vary in luminosity and color evolution depending on, among other properties, the merger's progenitors (e.g., BNS or NSBH), component masses, and remnant. Final outcomes to a BNS merger span a prompt BH collapse, a short-lived ($\sim$100 ms) differentially rotating hypermassive NS (HMNS), a longer-lived ($\gtrsim$10 s) rigidly rotating supramassive NS (SMNS; Shibata & Hotokezaka 2019), and a stable infinite-lifetime NS (Kasen et al. 2015; Margalit & Metzger 2019). If an NS remnant is born with a large magnetic field (a "magnetar"), it may impart additional energy on the ejected material (Metzger & Piro 2014; Gao et al. 2017; Metzger 2019; Fong et al. 2021). In addition, parameters such as the viewing angle, progenitor mass ratio, spins, and magnetic field strengths are all expected to result in observed kilonova light-curve diversity (Just et al. 2015; Metzger et al. 2018).

Concurrent with new discoveries by GW facilities in the nearby universe, short GRB detections have provided a large population of BNS or NSBH mergers at cosmological distances ($z \approx 0.1$–2.2; Berger 2014; Fong et al. 2017; Paterson et al. 2020). Short GRBs discovered by the Neil Gehrels Swift Observatory (Swift; Gehrels et al. 2004) have been followed up with deep optical and NIR observations for the past 15 yr, primarily to analyze their collimated, nonthermal afterglows (Fong et al. 2015). Despite their comparatively large distances, the wealth of optical and NIR follow-up of short GRBs provides unique and valuable information on potential kilonova emission. Indeed, some previous works have used short GRB detections to identify kilonova candidates from late-time excesses of mostly nearby ($z \lesssim 0.5$) bursts (Berger et al. 2013; Tanvir et al. 2013a; Jin et al. 2015; Yang et al. 2015; Gao et al. 2017; Kasliwal et al. 2017b; Gompertz et al. 2018; Lamb et al. 2019; Troja et al. 2019; Rossi et al. 2020b; Fong et al. 2021; O'Connor et al. 2021). To detect kilonova candidates in optical imaging, these studies have the added challenge of disentangling emission from thermal kilonovae and nonthermal afterglows. Additional work has explored the colors, ejecta masses (M_{ej}), velocities (V_{ej}), and lanthanide abundances (X_{lan}) of candidates (Ascenzi et al. 2019).

If all candidates claimed in previous works are indeed kilonovae, the population demonstrates significant diversity, especially considering that they are uniformly observed from a pole-on orientation given the detections of short GRBs. The advantage of inferring kilonova properties from short GRBs is that it removes the effects of viewing angle, implying that the candidates' observed variation is due to the diversity of kilonovae themselves (or potentially jet/kilonova interaction). A focus on deep upper limits allows us to circumvent the additional uncertainties imposed by modeling afterglows while still exploring kilonova diversity and bring in a much larger population of viable constraining observations.

In this paper, we incorporate the wealth of published short GRB optical and NIR observations, as well as new, unpublished data. We add to previous samples by including observations of short GRBs at all redshifts as some optimistic kilonova models are indeed observable at $z > 0.5$. The kilonova with the best-sampled light curve, AT 2017gfo, and the wealth

of existing kilonova models provide an excellent baseline against which we can compare constraints from a large sample of short GRBs. In Section 2 we describe our comprehensive catalog of 85 short GRB observations. In Section 3, we investigate the diversity of the data by comparing our sample of observations to the light curves of AT 2017gfo, kilonova models, and past kilonova candidates. In Section 4 we use the deepest upper limits in our sample to make constraints on the ejecta mass and velocity parameter space for each event. Finally, in Section 5 we discuss the implications of our analysis and consider approaches to future short GRB kilonova searches. Unless otherwise stated, all observations are reported in AB mag units and corrected for Galactic extinction, and all times since burst (δt) are reported in the observer's frame. We use a standard cosmology of $H_0 = 69.6 \, \mathrm{km \, s^{-1} \, Mpc^{-1}}$, $\Omega_M = 0.286$, and $\Omega_{vac} = 0.714$ throughout this work (Bennett et al. 2014).

2. Observations and Data Analysis

2.1. Overall Sample Characteristics

We present optical and NIR observations of 85 bursts discovered from 2005 to 2020 in an updated catalog of short GRB observations that probe kilonova emission properties. We primarily draw from short GRBs ($T_{90} \lesssim 2$ s or classified by the Swift Burst Alert Telescope (BAT) catalog; Lien et al. 2016) detected by BAT on board Swift. Four short GRBs in our sample have extended emission in their γ-ray light curves (Lien et al. 2016). One burst, GRB 060614, is classified as a long-duration GRB, with $T_{90} \sim 100$ s (Parsons et al. 2006; Jespersen et al. 2020), but lacked an accompanying supernova ruling out a massive star origin (Della Valle et al. 2006; Gal-Yam et al. 2006; Gehrels et al. 2006). We consider nine bursts in our sample to be kilonova candidate events.

We incorporate observations of 39 bursts with known redshifts across the full redshift range ($z \approx 0.1$–2.2). We note that all of these redshifts originate from the most probable host galaxy of each burst. While these associations are all based on low probability of chance coincidence values of $P_{cc} < 0.01$–0.15 (Bloom et al. 2002), it is still possible that not all host assignments are correct. We also include data for 46 bursts with unknown distances, for which we assume $z = 0.5$,[11] the approximate median redshift of Swift short GRBs (Berger 2014; Fong et al. 2017; Paterson et al. 2020; see Section 3.3 for implications of this assumption). We note one burst, GRB 150424A, for which multiple redshifts have been claimed ($z = 0.3$, Castro-Tirado et al. 2015; $z = 1$, Knust et al. 2017; Jin et al. 2018). Given the current uncertainty in redshift, we employ $z = 0.5$ in our analysis.

We draw optical and NIR observations from three sources: (i) unpublished observations that mainly comprise deep upper limits (Section 2.2), (ii) deep upper limits from GCN circulars that have not been otherwise published in the literature (Section 2.3), and (iii) published observations (or reanalyses of published observations) of past short GRBs, some of which have also been included in previous samples (Section 2.4). Notably, this work introduces 55 unpublished observations and over 40 deep upper limits from GCNs. In total, we include observations of 85 bursts, representing most of the Swift GRBs with $T_{90} \lesssim 2$ s or extended emission detected to date.

---

[11] With the exception of GRB 180418A, for which we assume $z = 1.0$, following the analysis in Rouco Escorial et al. (2021).

Observations span $\delta t = 0.003$–12 days post-burst (where δt is the time since the burst trigger) and the optical and NIR bands (*ugrizYJHK*). All observations are listed in the Appendix, Table A1.

2.2. Unpublished Observations

We start with new observations of 23 bursts, the majority of which have confirmed X-ray or optical afterglows that provide localization at the $\lesssim 1''$–$3''$ level. Three bursts lack X-ray afterglow detections, and our observations of these BAT positions, typically a few arcminutes in uncertainty, have all or partial optical coverage (observations with partial coverage are noted in Table A1).

We obtained these observations with the 8 m twin Gemini-North and Gemini-South telescopes, the 6.5 m MMT, the 6.5 m Magellan/Baade and Clay telescopes, the 4.2 m William Herschel Telescope (WHT), and the 3.8 m United Kingdom Infrared Telescope (UKIRT). We apply bias, flat-field, and dark corrections when relevant using standard tasks in the IRAF/ `ccdproc` package, as well as custom Python pipelines.[12] To align and co-add individual exposures, we use tools in IRAF and astropy (`CCDProc` and `Astroalign`; Tody 1993; Beroiz et al. 2020). We then register the co-added images to an absolute astrometric catalog using `astrometry.net` (Lang et al. 2010) or standard IRAF tasks to the Sloan Digital Sky Survey (SDSS) or USNO-B1 (for optical images; Monet et al. 2003; Alam et al. 2015) and the Two Micron All Sky Survey (2MASS; for NIR images; Skrutskie et al. 2006) catalogs.

For most bursts, we obtained a series of observations with the initial set typically at $\delta t \lesssim 3$ days, followed by one to three additional observations spanning timescales of $\delta t = 1$–12 days. For each burst, we perform relative astrometry between the initial image and each of the later sets using `Astroalign`. To uncover or place limits on transient emission on these timescales, we perform digital image subtraction using the `HOTPANTS` software package (Becker 2015).

If an optical or NIR source is detected within the GRB localization regions (Evans et al. 2009; Lien et al. 2016), we perform aperture photometry on the residual images to determine the source brightness using the IRAF/`phot` package. We determine zero-points by using point sources in common with the SDSS Data Release 12 (Alam et al. 2015), Pan-STARRS DR1 and DR2 (Chambers et al. 2016), and 2MASS (Skrutskie et al. 2006) or USNO-B1 (Monet et al. 2003) catalogs. If there are no significant residuals at or near the localization region, we obtain an upper limit from sources detected at 3σ significance in the field. As we obtain the limit from the initial image, our values do not include additional noise from the subtraction. In total, we present 52 unpublished upper limits and three unpublished detections of 23 bursts, 10 with known redshifts (Table A1).

2.3. Observations from GCNs

We search the GCNs of all short GRBs detected between 2013 and 2020 for constraining upper limits to ensure that our catalog covers all Swift short GRBs to date (2005–2013 is covered by the literature sample in Section 2.4). Considering that the range of peak kilonova luminosities based on models is $\nu L_\nu \approx (1$–$5) \times 10^{42}$ erg s^{-1} ($\sim$10 times the peak luminosity of

AT 2017gfo; see Figure 1), we only include data that could feasibly fall into the range of kilonova luminosities, or fainter than a given depth, corresponding to $griz \gtrsim 22.5$ mag and $JHK \gtrsim 21.0$ mag (AB system) at $z \approx 0.25$. We choose $z \approx 0.25$, as 80% of known redshifts in our sample fall above this cut. Observations significantly brighter than this are not included, as they are likely dominated by afterglow emission. In total, we collect deep optical and NIR limits of 18 bursts, seven with confirmed redshifts, from the GCNs (Table A1).

2.4. Published Observations

To incorporate the full sample of constraining short GRB observations, we undertake a literature search of all relevant short GRBs since 2004. The majority of bursts in this sample were discovered by Swift-BAT, with the exception of two bursts found by the INTEGRAL (GRB 131224A; Mereghetti et al. 2003), Fermi, and Suzaku telescopes (GRB 140619B; Yamaoka et al. 2006; Collaboration 2017). We begin by gathering observations from the catalog presented in Fong et al. (2015). In addition, we retrieve Hubble Space Telescope (HST) observations from the archive for GRB 160624A (also published in O'Connor et al. 2021). We also collect optical and NIR observations of recently published (2015–present) short GRBs at $\delta t \lesssim 12$ days.

Finally, we gather relevant detections and upper limits of short GRBs for which kilonovae have been claimed. These kilonova candidate bursts[13] are GRB 050709 (Jin et al. 2016), GRB 050724A (Gao et al. 2017), GRB 060614 (Yang et al. 2015), GRB 070714B (Gao et al. 2017), GRB 070809 (Jin et al. 2020), GRB 130603B (Berger et al. 2013; Tanvir et al. 2013a), GRB 150101B (Troja et al. 2018), GRB 160821B (Kasliwal et al. 2017b; Lamb et al. 2019; Troja et al. 2019), and GRB 200522A (Fong et al. 2021). Though a magnetar-powered kilonova has been claimed for GRB 080503 (Perley et al. 2009; Bucciantini et al. 2012), we do not include this burst as a kilonova candidate owing to the uncertainty in the burst's redshift and thus optical luminosity (Perley et al. 2009; Fong & Berger 2013). Assuming $z = 0.5$ for GRB 150424A, we also find luminous ($\gtrsim 10^{41}$ erg s^{-1}) optical and NIR detections beyond afterglow-length timescales ($\delta t \gtrsim 5$ days), motivating us to include these observations for completeness (although we do not consider it a kilonova candidate). Including these observations in our literature sample allows us to compare diverse models to the landscape of short GRBs with optical or NIR excesses that have been interpreted as kilonovae.

Though we apply the analysis in Section 3 to all observations from Fong et al. (2015) and the literature, in Table A1 we present a catalog of only (i) detections that have been interpreted as kilonovae, (ii) deep ($\gtrsim 21.5$ mag) upper limits (see justification of GCN upper limit magnitude cutoff; Section 2.3), and (iii) low-luminosity afterglow detections (less than the corresponding luminosity of AT 2017gfo; $\nu L_\nu \lesssim 5 \times 10^{41}$ erg s^{-1}).

---

[12] https://github.com/CIERA-Transients/Imaging_pipelines/

[13] We note that Gao et al. (2017) also claim that GRB 061006 had a detected kilonova. However, following Rossi et al. (2020b), we do not include this candidate in our sample, as optical detections at $\delta t \gtrsim 1$ day are likely dominated by host galaxy light (D'Avanzo et al. 2009).
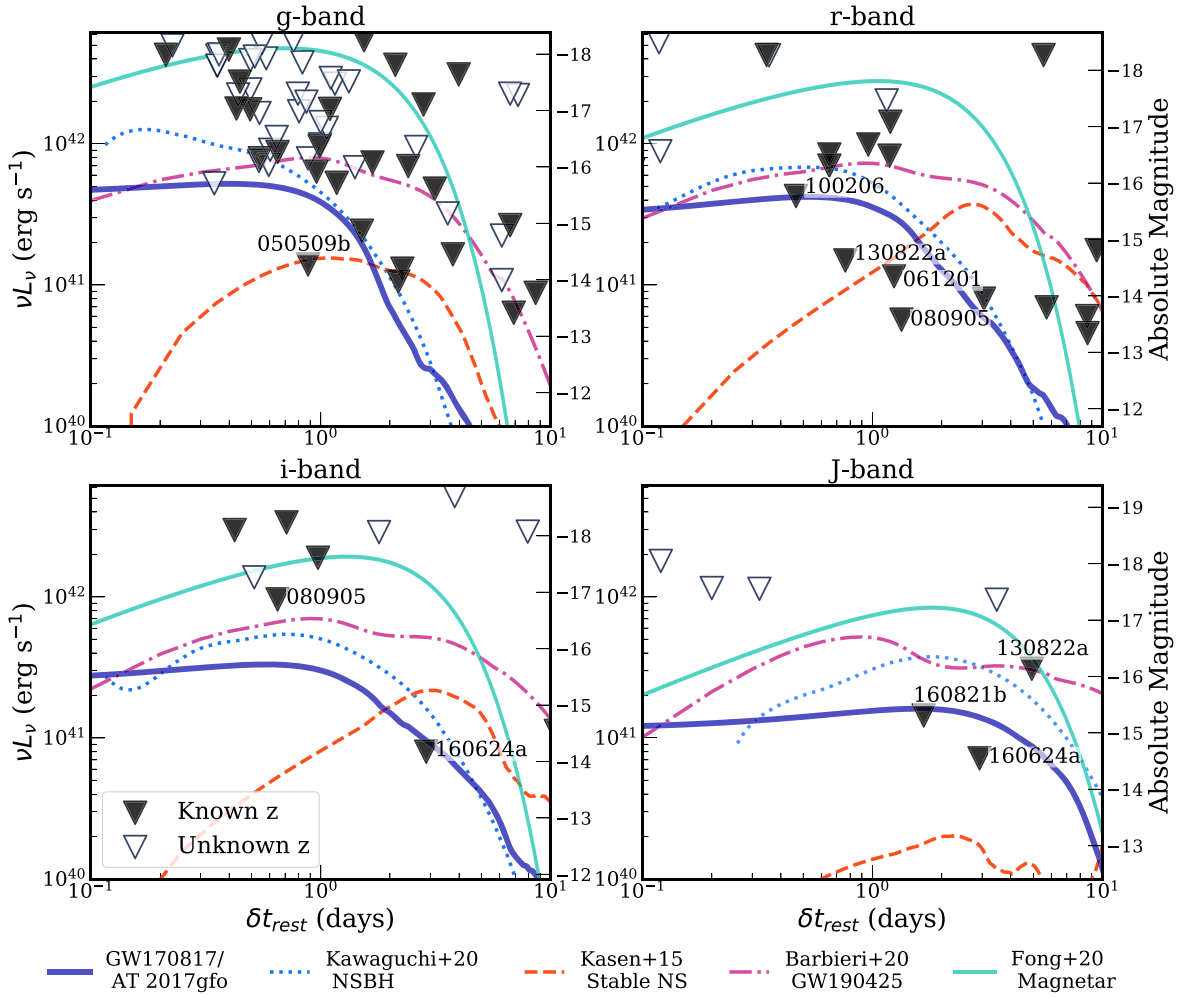
Figure 1. Light curves of AT 2017gfo and four diverse kilonova models considered in this work in the *griJ* bands. Light curves are shown in νL_ν (left y-axis) and absolute magnitude (right y-axis) units, and rest-frame time in days. In each panel, we show the interpolated, smoothed AT 2017gfo data set (solid dark-blue line; Villar et al. 2017), an NSBH kilonova model (blue dotted line; Kawaguchi et al. 2020b), an infinite-lifetime NS remnant kilonova model (red dashed line; Kasen et al. 2015), an extreme optimistic magnetar-boosted kilonova model (turquoise solid line; Fong et al. 2021), and a model for an optimistic scenario motivated by GW190425 (magenta dashed–dotted lines; Barbieri et al. 2020). Black and open triangles denote upper limits of short GRBs with known and unknown redshifts, respectively, in the respective rest-frame bands at $\delta t_{\rm rest} = 0.1$–10 days. The most constraining limits of bursts with known redshifts are labeled. The largest number of constraining limits appear in the *g* band (top left panel), typical of afterglow searches.

3. Comparisons between Short GRB Luminosities and Kilonova Models

We now explore our short GRB observational catalog in the context of an AT 2017gfo-like kilonova and three kilonova models. Our sample is fairly heterogeneous, spanning a range of observing bands, redshifts, and timescales. To enable direct comparisons of our observations to both AT 2017gfo and kilonova models, we use the bursts' redshifts to determine luminosities (or luminosity limits), approximate rest-frame bands, and rest-frame times after the burst ($\delta t_{\rm rest}$). We apply the following analyses to all observations in Table A1. As all observations were obtained as follow-up to short GRBs, we assume an approximately fixed viewing angle.

3.1. Comparison to AT 2017gfo

First, we compare our sample to the multiband light curves of AT 2017gfo at $d_L \approx 40.7$ Mpc (Cantiello et al. 2018). The published multiband data set of AT 2017gfo is well sampled for $\delta t_{\rm rest} \lesssim 12$ days and is compiled in Villar et al. (2017) with observations from Andreoni et al. (2017), Arcavi et al. (2017),

Coulter et al. (2017), Cowperthwaite et al. (2017), Díaz et al. (2017), Drout et al. (2017), Evans et al. (2017), Hu et al. (2017), Kasliwal et al. (2017a), Lipunov et al. (2017), Pian et al. (2017), Shappee et al. (2017), Smartt et al. (2017), Tanvir et al. (2017), Troja et al. (2017), Utsumi et al. (2017), Valenti et al. (2017), and Pozanenko et al. (2018). In each of the *grizYJHK* bands, we linearly interpolate to 1 hr bins to create finer sampling and smooth using a Savitsky–Golay filter with a time resolution of $\sim$1–6 days, producing master light curves of an AT 2017gfo-like kilonova. We show our interpolated and smoothed AT 2017gfo light curves as blue solid lines in Figure 1.

We calculate the ratio, $\mathcal{R}$, of the luminosity of each observation to that of the AT 2017gfo-like light curves in the nearest rest-frame band and time, where $\mathcal{R} \equiv \nu L_\nu({\rm sGRB})/\nu L_\nu({\rm AT\,2017gfo})$. Due to the large apparent redshift of sGRBs at cosmological distances, $\nu({\rm sGRB})$ is approximately but not exactly $\nu({\rm AT\,2017gfo})$. This method effectively normalizes each short GRB observation by the smoothed light curves, enabling us to directly compare detections and limits across different bands and timescales. We note that this is an approximation used in the context of a large sample. To quantify the potential uncertainty, we use a model of the
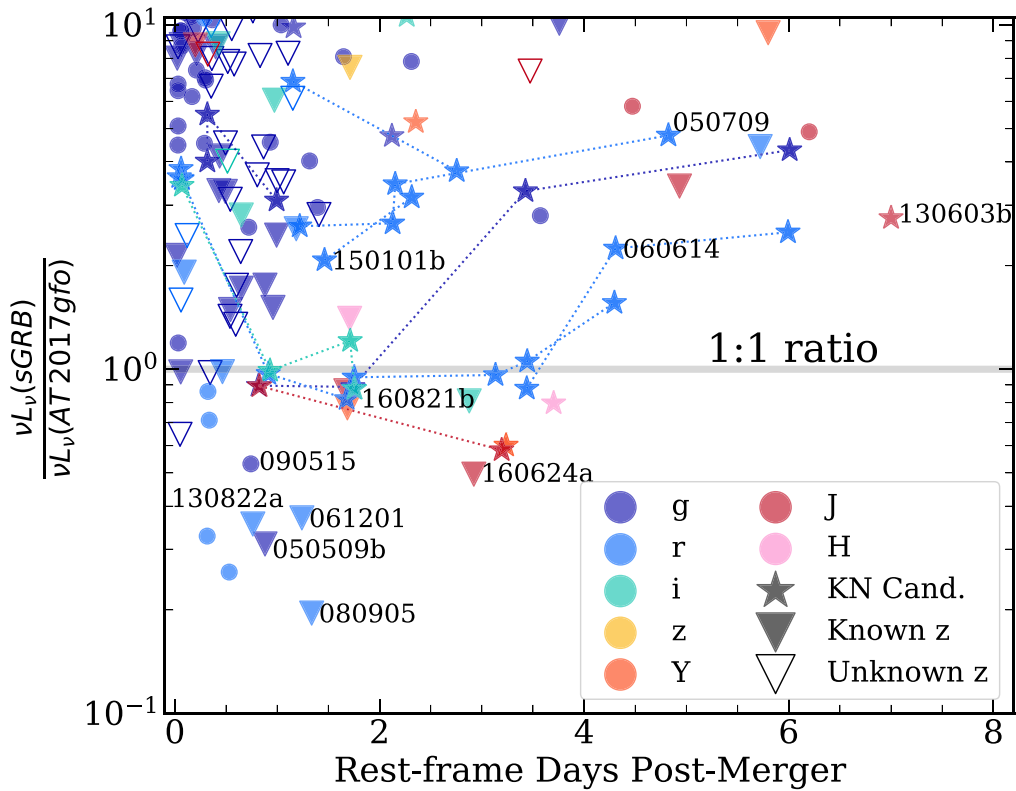
Figure 2. The ratios, $\mathcal{R}$, of short GRB observations to the AT 2017gfo light curves, matched in rest-frame time and approximate rest-frame band, in νL_ν units (see Section 3.1 for ratio method). Filled triangles represent upper limits of bursts with known redshift, and open triangles show upper limits of bursts with unknown redshift. Only the deepest upper limit of each short GRB is shown. Circles denote afterglow detections, and stars represent kilonova candidate detections. For kilonova candidates with multiple detections in a single band, stars are connected with dotted lines. The color of each symbol corresponds to the approximate rest-frame band (spanning the *grizyJH* bands) of each observation. Deep upper limits of 10 bursts spanning $\delta t_{rest} = 0.05$–3 days and the *griyJ* bands probe luminosities below AT 2017gfo. We label the GRB names of markers denoting some upper limits with $\mathcal{R} \lesssim 0.8$, relevant kilonova candidates, and low-luminosity afterglows. The gray horizontal line represents a 1:1 ratio against which each short GRB observation can be independently compared. The majority of kilonova candidate detections, including those of GRB 050709, GRB 060614, GRB 130603B, GRB 150101B, and GRB 200522A, have $\mathcal{R} \gtrsim 1$ values.

AT 2017gfo spectral energy distribution (SED) discussed in Kasen et al. (2017). The model SED allows us to approximate the luminosity of AT 2017gfo at the true rest-frame wavelength of each short GRB observation at $\delta t < 8$ days and compare this value to that used in our analysis. We find that the median errors of our AT 2017gfo luminosities due to this transformation and across all bands range from 3% to 37%. The largest median uncertainties are of rest-frame *g*-band observations, likely due to the rapid SED evolution of AT 2017gfo in the bluest bands. We note that the alternative approach to our ratio method, modeling the spectral evolution of AT 2017gfo, would add uncertainties to the $\mathcal{R}$ values, though these uncertainties are likely to be smaller than those of our method. In Figure 2, we plot $\mathcal{R}$ as a function of rest-frame time, δt_{rest}.

This analysis increases the number of short GRBs whose kilonovae must be less luminous than AT 2017gfo. The constraining upper limits span $\delta t_{rest} \approx 0.05$–3 days and are mostly in the bluer rest-frame bands, a product of typical optical afterglow searches and the required shifting of rest-frame-equivalent bands to bluer wavelengths. From their samples of <40 short GRBs, previous works found six bursts (GRB 050509B, GRB 051210, GRB 061201, GRB 080905A, GRB 100206, and GRB 160624A), which have deep upper limits able to rule out an AT 2017gfo-like kilonova (Gompertz et al. 2018; Rossi et al. 2020b; O'Connor et al. 2021). We corroborate these findings, except for GRB 051210, for which we consider a higher-redshift estimate than previous studies ($z \gtrsim 1.55$; Berger 2007), thus yielding significantly less

constraining limits. We find an additional five short GRBs with upper limits lower than or nearly comparable to an AT 2017gfo-like kilonova ($\mathcal{R} \lesssim 1$; GRB 130822A, GRB 150120A, and GRB 160821B with known redshifts, and GRB 080503 and GRB 140516 assuming $z = 0.5$). However, GRB 160821B is a known kilonova candidate (Kasliwal et al. 2017b; Lamb et al. 2019; Troja et al. 2019), highlighting differences in the luminosities and colors as compared to AT 2017gfo.

In the context of the handful of short GRBs with claimed kilonovae in the literature (GRB 050709, GRB 050724A, GRB 060614, GRB 070714B, GRB 070809, GRB 130603B, GRB 150101B, GRB 160821B, and GRB 200522A; Berger et al. 2013; Tanvir et al. 2013a; Yang et al. 2015; Jin et al. 2016; Gao et al. 2017; Kasliwal et al. 2017b; Jin et al. 2018; Troja et al. 2018; Lamb et al. 2019; Troja et al. 2019; Jin et al. 2020; Fong et al. 2021; O'Connor et al. 2021), Figure 2 demonstrates that their late-time excesses ($0.5 < \mathcal{R} < 10$) exhibit significant diversity in their luminosities and colors. We reconfirm the findings of previous works that the detections of most kilonova candidate bursts have values $\mathcal{R} \gtrsim 1$ in the rest-frame optical band (Gompertz et al. 2020b; Rossi et al. 2020b; Fong et al. 2021). More specifically, only GRB 050709, GRB 060614, GRB 130603B, and GRB 160821B had some detections at $\delta t_{rest} > 2$ days with comparable luminosities to AT 2017gfo ($\mathcal{R} \approx 0.8 - 3$). The remaining kilonova candidates had more luminous detection ratios ($\mathcal{R} \gtrsim 3$) at $\delta t_{rest} > 2$ days (GRB 050724A, GRB 150101B, GRB 200522A) or detections

only at early times ($\delta t_{\rm rest} < 1.5$ days; GRB 070714B, GRB 070809), when extricating afterglow emission is particularly difficult.

Finally, we reconfirm the sub–AT 2017gfo ($\mathcal{R} < 1$) luminosity of the early detections of GRB 061201, GRB 080905A, and GRB 090515 found previously (Rossi et al. 2020b). The detections of most of these bursts can be explained by their proximal distances, as these three bursts all have low redshifts ($z \lesssim 0.4$; Stratta et al. 2007; Rowlinson et al. 2010a, 2010b), Taken together, these low-luminosity afterglow detections, brighter kilonova candidate detections, and constraining upper limits demonstrate that there is a wide diversity in kilonovae observed at a pole-on viewing angle.

3.2. Comparisons to Pole-on Kilonova Models

Motivated by the diversity of kilonova models and the variety of BNS or NSBH merger progenitors discovered by GW detectors (e.g., GW190425, GW190814, Abbott et al. 2020a, 2020b), we extend our comparative analysis to a set of kilonova models from the literature representing a variety of short GRB progenitors and remnants. Each of the models chosen for our comparisons possesses unique observable signatures that can be tied to the mergers' progenitors and remnants.

In addition to the BNS merger kilonova, GW170817, we employ an NSBH merger kilonova model to represent a second potential progenitor channel for short GRBs (Kawaguchi et al. 2020b). In addition, we consider two models of optimistic, if infrequent, outcomes to a BNS or NSBH merger. These are an infinite-lifetime NS remnant to a BNS merger (Kasen et al. 2015) and a massive BNS merger modeled by the parameters of the unusual event, GW190425 (Abbott et al. 2020a; Barbieri et al. 2020). As the detection of a short GRB automatically provides on-axis (or close to on-axis) orientation, we choose models for pole-on orientations when available.

While the overall colors of NSBH merger kilonovae are expected to be redder, the amount of ejecta emitted is variable and depends on several factors, including the BH spin, mass ratio, and NS properties (Rosswog 2005; Just et al. 2015; Kyutoku et al. 2015; Foucart et al. 2018; Shibata & Hotokezaka 2019). Indeed, potentially only a small fraction of NSBH mergers produce EM emission (Broekgaarden et al. 2021). Here, a kilonova is composed of (i) lanthanide-rich dynamical ejecta created by tidal interactions and (ii) post-merger material ejected from the accretion disk formed around the remnant object (Metzger et al. 2008, 2009). For comparison to our short GRB catalog, we choose a representative NSBH model, parameterized by dynamical ejecta $M_{\rm ej} = 0.02~M_\odot$ and $Y_{\rm e} = 0.09$–0.11 and post-merger ejecta $M_{\rm ej} = 0.04~M_\odot$ and $Y_{\rm e} = 0.1$–0.3 (Kawaguchi et al. 2020b). This model uses a restricted line list to calculate ejecta opacities (resulting in an error of $\lesssim 0.2$ mag) and describes a kilonova viewed at pole-on orientation. We note, however, that due to uncertainties in the opacities of highly ionized elements expected in the ejecta at $\delta t < 1$ day, the light curves' luminosity may be artificially enhanced on these timescales (Kawaguchi et al. 2020a). Using supplied $grizJHK$-band models, we calculate $\mathcal{R} \equiv \nu L_\nu$ (sGRB)$/\nu L_\nu$(NSBH Model) and find that upper limits of 13 short GRBs, nine with known redshifts, at $\delta t_{\rm rest} < 7$ days have $\mathcal{R} < 1$ (Figure 3, top left panel).

We next compare deep upper limits of short GRBs to a model for an infinite-lifetime NS remnant (Kasen et al. 2015). A long-lived NS remnant will inject energy into the post-merger disk, increasing the amount and electron fraction of disk ejecta material (Dessart et al. 2009; Perego et al. 2014; Lippuner et al. 2017; Fahlman & Fernández 2018; Radice et al. 2018). We employ a model at a pole-on orientation (cos (θ) = 0.95) with a disk mass $M_{\rm disk} \sim 0.03~M_\odot$ using supplied $grizyJHK$-band light curves (Kasen et al. 2015). As these model light curves rise more slowly than AT 2017gfo (Figure 1), upper limits at $\delta t \lesssim 2$ days are less constraining. Upper limits of six bursts at 0.8 days $\lesssim \delta t_{\rm rest} < 9$ days are able to rule out this model.

In Figure 3, we display cumulative distributions of $\mathcal{R}$-value upper limits with respect to the data and two models, including only the minimum $\mathcal{R}$ value of a given short GRB in each distribution. It is clear that of three distributions, our catalog is most constraining for the NSBH model and least constraining for the infinite-lifetime NS remnant model.

Finally, we briefly compare to a model for the unusually massive GW-detected BNS merger, GW190425 (Abbott et al. 2020a), parameterized by the event's component masses (Barbieri et al. 2020). This model assumes a BNS merger employing the DD2 NS equation of state (Hempel & Schaffner-Bielich 2010; Typel et al. 2010), resulting in a kilonova more luminous than AT 2017gfo. However, we note that alternate scenarios have been proposed in which the emission is predicted to be much fainter (Foley et al. 2020; Kyutoku et al. 2020). Thus, the Barbieri et al. (2020) model considered here represents an optimistic outcome for this event, especially at times $\delta t \gtrsim 1$ day (Figure 1). Subsequently, limits of 14 bursts rule out this model ($\mathcal{R} < 1$).

3.3. Implications of Ratio Analysis and Assumptions

We first explore the implications of our assumption of a fiducial redshift ($z = 0.5$, the median value of Swift short GRBs) to the bursts with unknown redshifts of our sample. We note that some bursts with unknown redshifts may have very faint or unidentified host galaxies and thus may be more likely to be at redshifts higher than the observed median, while others may exist at large offsets from their hosts, making precise host identifications based on chance alignment difficult. Higher assumed redshifts undoubtedly affect the constraining power of the sample. For instance, assuming $z = 0.5$, upper limits of 2 and 23 bursts have values of $\mathcal{R}_{\rm AT\,2017gfo} < 1$ and $\mathcal{R}_{\rm AT\,2017gfo} < 10$, respectively. If we instead employ $z = 1$ (a conservative estimate) for these bursts' redshift, these numbers drop to 0 and 7, respectively. However, these bursts are included for completeness of the catalog and may have redshifts identified at a later time. Given this caveat, we find that the most meaningful constraints on short GRB kilonovae come from low-redshift bursts, naturally a result of the smaller luminosity distances and the decreased blue-shifting of the observed filters. The eight bursts with upper limits of lower luminosities than AT 2017gfo span the redshift range $0.111 \lesssim z \lesssim 0.483$.

The majority of kilonova candidates are nearby ($z \lesssim 0.5$) and have larger optical luminosities and bluer colors than AT 2017gfo (likely viewed at $\sim 20°$ off-axis; Mooley et al. 2018; Ghirlanda et al. 2019; Hotokezaka et al. 2019; Margutti & Chornock 2020), which can partially be explained by Malmquist bias (implying that we must be probing the upper end of the kilonova luminosity function with short GRBs). Viewing angle may also contribute to the bluer colors, as, generally, lanthanide-rich dynamical ejecta is concentrated in the equatorial regions, a result of the tidal tails, while lanthanide-poor emission is distributed isotropically, resulting
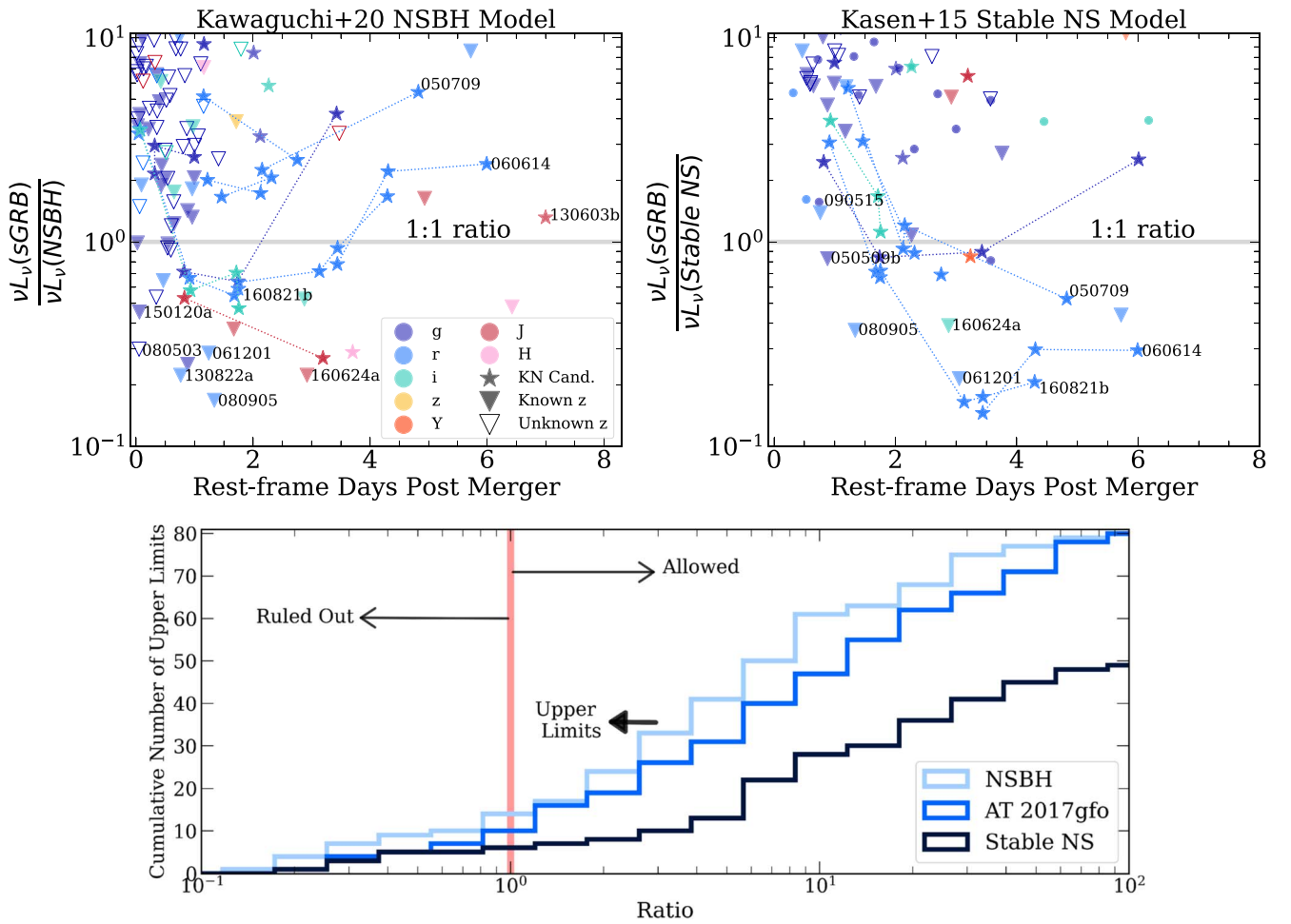
Figure 3. Top row: same as Figure 2, but $\mathcal{R}$ compared to an NSBH model (left; Kawaguchi et al. 2020b) and an infinite-lifetime NS remnant kilonova model (right; Kasen et al. 2015). Overall our limits have more constraining power on the NSBH model than AT 2017gfo, especially in the NIR bands. Since the infinite NS remnant kilonova model peaks later and at lower luminosities than AT 2017gfo (Figure 1), fewer limits rule out this model than either AT 2017gfo or the NSBH case. Bottom: cumulative distributions of luminosity ratio, $\mathcal{R}$, values derived from short GRB upper limits of AT 2017gfo (blue), the NSBH model (light blue), and the infinite NS remnant model (dark blue). Only the deepest limit of each burst is included in the distribution. Thus, the cumulative number of upper limits can be thought of as the number of bursts with upper limits that rule out a factor of $\mathcal{R}$ of each model. The vertical line denotes $\mathcal{R} = 1$, below which the limit can rule a model out. The NSBH model is ruled out ($\mathcal{R} \lesssim 1$) by 13 upper limits, the largest number of the three models shown.

in bluer emission at the poles (Wanajo et al. 2014; Sekiguchi et al. 2015; Metzger et al. 2018; Piro & Kollmeier 2018). Further observations of on-axis (short GRB) and off-axis (GW-detected) BNS/NSBH mergers will investigate the extent to which viewing angle plays a role in observed kilonova colors.

Turning to NSBH merger kilonovae, which in general are expected to be redder, the few existing NIR limits at $\gtrsim 1.9$ days offer more constraining power ($\mathcal{R}_{\rm NSBH} < \mathcal{R}_{\rm AT\,2017gfo}$) than for AT 2017gfo-like kilonovae. Moreover, the single HST F160W detection of GRB 130603B more closely traces our NSBH model and is a factor of ≈ 3 in excess of AT 2017gfo, in line with previous assessments that this burst is consistent with an NSBH merger kilonova (Hotokezaka et al. 2013; Kawaguchi et al. 2016). While there are optical luminosity differences between the AT2017gfo and the NSBH model considered here, they primarily reside at $\delta t \lesssim 1$ day, when the afterglow would dominate over any kilonova emission. There is potentially a wide diversity in NSBH binary spins and mass ratios (as inferred from, e.g., GW systems; Abbott et al. 2021) that, if true, imply a wider range in luminosities for NSBH kilonovae than those of BNS mergers (in the absence of a long-lived remnant; Just et al. 2015; Shibata & Hotokezaka 2019). Indeed,

these model comparisons highlight the need for deep, NIR-band follow-up at $\delta t \gtrsim 1$ day to distinguish between canonical BNS and NSBH kilonova models following on-axis short GRBs.

Our catalog is also well suited to probe a model that predicts bluer overall colors, as 90% of the upper limits in our sample are in the rest-frame *gri* bands. In the long-lived NS remnant scenario, which is expected be rare ($\lesssim 3\%$ of all BNS mergers are expected to result in a stable NS remnant; Margalit & Metzger 2019), the kilonova exhibits a slower rise (Kasen et al. 2015). Thus, only rest-frame *r*- and *i*-band observations at $\delta t \gtrsim 2$ days, where our catalog is fairly sparse, are comparatively meaningful.

The current short GRB catalog offers significant constraining power on high-luminosity kilonova models, such as the "magnetar-boosted" model used to explain the luminous kilonova candidate GRB 200522A (Fong et al. 2021), of which $\sim 50\%$ of our limits are constraining. Moreover, motivated by the discovery of the high-mass BNS merger GW190425 (total mass of 3.4 $M_\odot$; Abbott et al. 2020a), there are a number of models describing the event's kilonova that range in predicted luminosities by a factor of ≈ 25. These

Table 1
Median Constraining Upper Limit of Kilonova Ejecta Mass by Burst and Electron or Lanthanide Fraction

GRB	z	Median Constraining $M_{\rm ej}$ (M19)			Median Constraining $M_{\rm ej}$ (K17)		
		$Y_{\rm e} = 0.15$ ($M_\odot$)	$Y_{\rm e} = 0.40$ ($M_\odot$)	$Y_{\rm e} = 0.45$ ($M_\odot$)	$X_{\rm lan} = 10^{-2}$ ($M_\odot$)	$X_{\rm lan} = 10^{-4}$ ($M_\odot$)	$X_{\rm lan} = 10^{-9}$ ($M_\odot$)
050509B	0.225	⋯	0.11	0.02	⋯	0.02	0.01
050906	0.5[a]	⋯	⋯	0.24	⋯	⋯	0.08
060502B	0.287	⋯	⋯	0.33	⋯	0.06	0.04
061201	0.111	⋯	0.07	0.02	0.06	0.02	0.01
080503	0.5[a]	⋯	⋯	0.40	⋯	0.1	0.08
080905A	0.122	⋯	0.09	0.02	⋯	0.01	0.01
090305	0.5[a]	⋯	⋯	0.40	⋯	⋯	⋯
091109B	0.5[a]	⋯	⋯	0.33	⋯	⋯	0.08
100206	0.407	⋯	0.40	0.09	⋯	0.03	0.02
130822A	0.154	⋯	0.04	0.01	⋯	0.02	0.02
140516	0.5[a]	⋯	⋯	0.40	⋯	0.06	0.03
150120A	0.46	⋯	⋯	⋯	⋯	⋯	0.10
160624A	0.483	0.11	0.05	0.04	0.03	0.02	0.04
180805B	0.661	⋯	⋯	0.40	⋯	⋯	⋯

Notes. Numbers show the median $M_{\rm ej}$ of constraining $M_{\rm ej}$–$V_{\rm ej}$ pairs at the fixed $Y_{\rm e}$ or $X_{\rm lan}$ value. The three left columns show constraints on the grid of models created using analytical prescriptions of Metzger (2019; M19) and opacities from Tanaka et al. (2020). The right columns show constraints on the grid of models described in Kasen et al. (2017; K17). Dashes show bursts with no constraining $M_{\rm ej}$–$V_{\rm ej}$ pairs at the fixed $Y_{\rm e}$ or $X_{\rm lan}$ value.
[a] Redshift unknown, $z = 0.5$ taken as fiducial value in analysis.

differences depend on assumptions of tidal deformability, component masses, and the survival of an NS remnant (Barbieri et al. 2020; Foley et al. 2020; Kyutoku et al. 2020). Adopting the optimistic Barbieri et al. (2020) model as a proof of concept, 25% of upper limits in our sample probe lower luminosities than this model.

4. Constraints on Kilonova Ejecta Properties

4.1. Model Grid Descriptions

We next determine how the short GRB catalog can place quantitative constraints on kilonova ejecta properties. In particular, we focus on constraints for the ejecta properties ($M_{\rm ej}$, $V_{\rm ej}$), as well as composition (electron fraction $Y_{\rm e}$ or lanthanide fraction $X_{\rm lan}$). We determine that deep upper limits with values $\mathcal{R}_{\rm AT\,2017gfo} \lesssim 3$ are capable of ruling out the extreme upper end of kilonova ejecta masses and velocities ($M_{\rm ej} = 0.5\ M_\odot$ and $V_{\rm ej} = 0.5c$), which we set as the criteria for subsequent analysis. Ultimately, we find that upper limits of 14 short GRBs, including nine bursts with known redshifts, fit these criteria (see Table 1).

Our goal is to translate each observation into a constraint on the $M_{\rm ej}$–$V_{\rm ej}$ parameter space at fixed values of $Y_{\rm e}$ or $X_{\rm lan}$. For this, we employ two approaches: direct comparison to a grid of models from Kasen et al. (2017, hereafter K17), and forward-modeling based on analytical prescriptions in Metzger (2019, hereafter M19). The K17 models are based on simulations that include time-varying opacity contributions based on atomic data from both the lighter and lanthanide material synthesized in the kilonova ejecta (Kasen et al. 2013).

Superimposed "blue" ($Y_{\rm e}$, $\gtrsim 0.25$) and "red" ($Y_{\rm e} \lesssim 0.25$) component models are often invoked to describe kilonova light curves (Kasen et al. 2017; Villar et al. 2017). As both components are dominated by thermal emission from radio-active decay (as in Arnett 1982), the blue, low-opacity kilonova light curves peak earlier in the optical band ($\lesssim 1$ day post-merger), while the red, high-opacity light curves peak later in the NIR band (1–2 days post-merger; e.g., AT 2017gfo;

Cowperthwaite et al. 2017; Kilpatrick et al. 2017; Villar et al. 2017). We consider each component separately in this analysis.

We retrieve the publicly available K17 grids of "red" lanthanide-rich ($X_{\rm lan} = 10^{-2}$), "blue" lanthanide-poor ($X_{\rm lan} = 10^{-4}$), and "extremely blue" ($X_{\rm lan} = 10^{-9}$) components.[14] An "extremely blue" component is a predicted product of a long-lived NS remnant (Lippuner et al. 2017). The model grids provide a range of $M_{\rm ej} = 0.001$–$0.1\ M_\odot$ and $V_{\rm ej} = 0.03c$–$0.3c$ for fixed $X_{\rm lan}$ values. The fine wavelength sampling ($\lesssim 0.04\ \mu$m) allows us to compare each short GRB observation directly to the relevant rest-frame wavelength. However, the $M_{\rm ej}$ and $V_{\rm ej}$ parameter space is coarsely sampled.

Thus, we generate a more finely spaced light-curve grid following the prescriptions in M19. Our models utilize the gwemlightcurves Python-based code (Coughlin et al. 2019, 2020), with updates for opacity based on the electron fraction ($Y_{\rm e}$) from simulations in Tanaka et al. (2020). We generate observed light-curve models at the redshifts of the 14 bursts used in this analysis (Table 1) for a range of ejecta masses and ejecta velocities. We calculate in-band light curves in the observer frame using pysynphot, a python-based synthetic photometry package (STScI Development Team 2013), accounting for all redshift and time dilation effects when the light curves are generated. The result is log-linear grids of 900 light-curve models spanning $M_{\rm ej} = 0.001$–$0.5\ M_\odot$ and $V_{\rm ej} = 0.03c$–$0.5c$ for $Y_{\rm e} = 0.15$ (a "red" component), $Y_{\rm e} = 0.40$ (a "blue" component), and $Y_{\rm e} = 0.45$ (an "extremely blue" component). We note that the M19 $Y_{\rm e}$ values do not directly correspond to the K17 values of $X_{\rm lan}$, so we include both models with their respective values for completeness. We note that the lack of time-varying opacities in this method leads to less constraining results (see Section 4.4 for a more thorough analysis of the differences between K17 and M19 models), although this allows for finer sampling of the $M_{\rm ej}$–$V_{\rm ej}$ grid and extension to larger values.

---

[14] https://github.com/dnkasen/Kasen_Kilonova_Models_2017
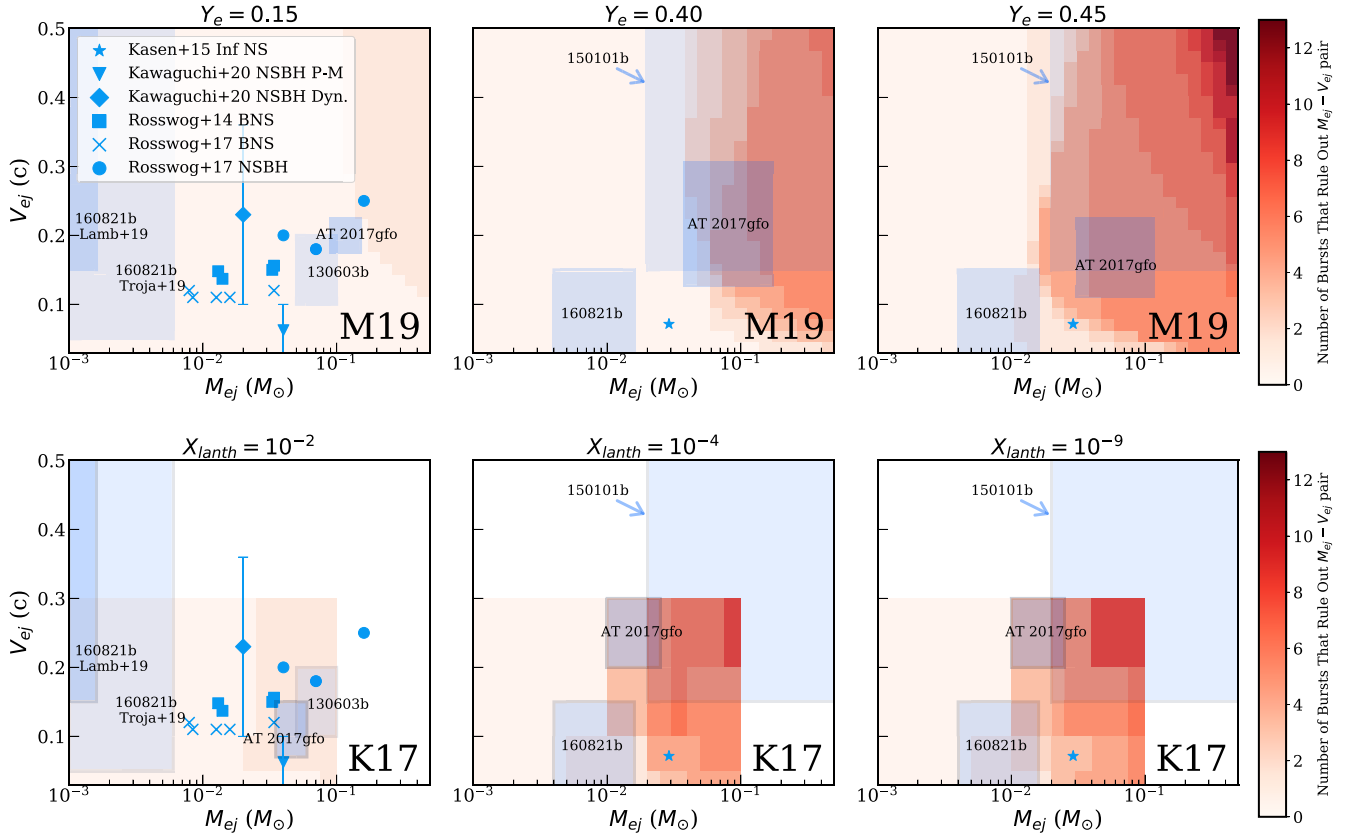
Figure 4. Constraints on the M_{ej}–V_{ej} parameter space using upper limits from 14 short GRBs for the M19 (top; Metzger 2019) and the K17 (bottom; Kasen et al. 2017) model grids. White space on the bottom row grids indicates that the K17 models do not extend to this parameter space. The red color map corresponds to the number of short GRBs for which an upper limit rules out a kilonova parameterized by the corresponding M_{ej}–V_{ej} pair. From left to right, the progression from redder to bluer components (values of Y_e and X_{lan} denoted) shows the larger constraining power of our catalog on a blue component, a product of the nature of our short GRB observations. The estimated ejecta values of three short GRB kilonova candidates (130603B; Barnes et al. 2016, 150101B; Troja et al. 2018, and 160821B; Lamb et al. 2019; Troja et al. 2019), as well as AT 2017gfo, are shown as blue regions that span the error bars of each analysis and are split into components when relevant. We also plot the dynamical ejecta parameters and the post-merger ejecta parameters of the models used in our ratio analysis (Kawaguchi et al. 2020b and Kasen et al. 2015), as well as the values for a suite of BNS and NSBH kilonova models of Rosswog et al. (2014, 2017) in their corresponding panels.

4.2. Quantitative Constraints on Ejecta Properties

Since each of the K17 and M19 light curves is parameterized by an M_{ej}–V_{ej} pair, we are able to use limits to constrain the allowed M_{ej}–V_{ej} space of each burst's kilonova. For each of the fixed values of Y_e or X_{lan}, we iterate through the model light curves to determine which M_{ej}–V_{ej} pairs are allowed or not allowed given the luminosity constraints imposed by each limit. If a given burst has multiple constraining observations, we determine the parameter space that is ruled out for each limit separately and then combine them into a single contour. In this manner, a given M_{ej}–V_{ej} pair only has be to ruled out once for a given burst in order to be ruled out entirely. In Figure 4 we show the resulting constraints of the 14 short GRBs considered on the K17 and M19 M_{ej}–V_{ej} parameter spaces. In Table 1, we list the median upper limit on the ejecta mass of constraining M_{ej}–V_{ej} pairs for each burst and component. As V_{ej} does not vary much over the range of ejecta masses considered, we do not make constraints, as it would be almost entirely based on the grid size (Figure 4).

In the red ($X_{lan} = 10^{-2}$) K17 grid, we find that upper limits of only two bursts (GRB 061201 and GRB 160624A) constrain the parameter space, limiting a red component to $M_{ej} < 0.06~M_\odot$. The K17 grid constraints of GRB 160624A ($M_{ej} \lesssim 0.04~M_\odot$) are consistent with those of a separate analysis (O'Connor et al. 2021). For blue and "extremely blue" kilonova components ($X_{lan} = 10^{-4}$

and $X_{lan} = 10^{-9}$, respectively), the number of limits that enter the K17 parameter space increases to 9 and 12 bursts, respectively, a natural consequence of the prevalence of deep, optical follow-up observations. The M19 grids overall give similar inferred properties (albeit less constraining), and 13 bursts are able to rule out a fast ($V_{ej} \gtrsim 0.4c$), massive ($M_{ej} \gtrsim 0.4~M_\odot$), "extremely blue" ($Y_e = 0.45$) component (Table 1 and Figure 4). Depending on the precise model, meaningful constraints span $M_{ej} \lesssim 0.01$–$0.1~M_\odot$.

4.3. Comparisons to Known Candidate Kilonovae and Simulation Parameters

For context, we include inferred ejecta property values from AT 2017gfo, kilonova candidates, and simulations in Figure 4. To determine the location of AT 2017gfo on the K17 grids, we use the inferred M_{ej}–V_{ej} parameters compiled in Siegel (2019) based on optical and NIR observations (Arcavi et al. 2017; Chornock et al. 2017; Cowperthwaite et al. 2017; Drout et al. 2017; Kasen et al. 2017; Kasliwal et al. 2017a; Kilpatrick et al. 2017; McCully et al. 2017; Nicholl et al. 2017; Perego et al. 2017; Pian et al. 2017; Smartt et al. 2017; Troja et al. 2017; Villar et al. 2017; Coughlin et al. 2018). These parameters span $V_{ej} \approx 0.2c$–$0.3c$ and $M_{ej} \approx 0.01$–$0.02~M_\odot$ for a red component ($X_{lan} \lesssim 10^{-4}$) and $V_{ej} \approx 0.07c$–$0.14c$ and $M_{ej} \approx 0.04$–$0.06~M_\odot$ for a blue component ($X_{lan} \approx 10^{-2}$–10^{-1}). To compare AT 2017gfo to the M19 grids, we select the best-fit model using χ^2-minimization between the

interpolated master light curves for AT 2017gfo and the grid of models for each Y_e value and wavelength (Figure 4). The ejecta properties for AT 2017gfo are determined in this manner to ensure a fair comparison to short GRBs in the context of this model grid.

We also place our ejecta property constraints from our short GRB limits in the context of inferred values of candidate short GRB kilonovae. We caution that exact values are subject to variations in data reduction methods and assumed afterglow and kilonova models. In total, the estimates span $0.001 \ M_\odot \lesssim M_{ej} \lesssim 0.1 \ M_\odot$ and $0.025c \lesssim V_{ej} \lesssim 0.9c$ or are upper limits (Barnes et al. 2016; Troja et al. 2018; Lamb et al. 2019; Troja et al. 2019). Analyses that describe the predicted ejecta mass as either red or dynamical ejecta are compared to the red component, while those that describe the ejecta as post-merger outflow or accretion disk winds are compared to our bluer components (e.g., Metzger & Fernández 2014; Perego et al. 2014). Compared to the inferred ejecta properties of AT 2017gfo and GRB 130603B, only a few bursts have limits that translate to comparable or lower values of M_{ej} (for a given V_{ej}).

Finally, we include theoretical predictions for the NSBH and infinite-lifetime NS remnant kilonova models considered earlier (Kasen et al. 2015; Kawaguchi et al. 2020b), as well as additional BNS and NSBH models that span a broad range of input parameters and physics (Rosswog et al. 2014, 2017). As the NSBH model's post-merger ejecta comprises $Y_e = 0.1$–0.3 material, we plot both the dynamical and post-merger ejecta parameters on the red component grids only (Kawaguchi et al. 2020b). Since the infinite-lifetime NS remnant model parameters do not include $Y_e < 0.25$ material (Kasen et al. 2015), we include this only on the bluer component grids. These three comparison sets, AT 2017gfo, short GRB kilonovae, and inferred values from simulations are all plotted in Figure 4.

This comparison yields several new constraints, although the M19 and K17 grids give slightly different results in terms of direct comparisons (model dependencies further explored in Section 4.4). Concentrating on the "red" component ejecta ($Y_e = 0.15$, $X_{lan} = 10^{-2}$), the M19 model constraints cannot rule out a red kilonova with properties similar to AT 2017gfo or any short GRB kilonovae. Furthermore, the GRB 160624A upper limits on the red K17 grid are deep enough to rule out the parameter space occupied by AT 2017gfo, GRB 130603B, and the NSBH models given in Rosswog et al. (2017). For the "blue" component ($Y_e = 0.40$, $X_{lan} = 10^{-4}$), upper limits of five bursts (GRB 050509B, GRB 061201, GRB 080905A, GRB 130822A, GRB 160624A) rule out most of the parameter space both allowed by the upper limit of GRB 150101B and estimated for AT 2017gfo, compared to ~ 3 (GRB 061201, GRB 130822A, GRB 160624A) which rule these out on the blue M19 grid. We find that four limits rule out the infinite-lifetime NS remnant kilonova parameters on the "extremely blue" K17 grid, while two rule out this model on the corresponding M19 grid.

Only one other compilation work has uniformly estimated short GRB kilonova ejecta masses to date (Ascenzi et al. 2019). With the exception of their analysis of GRB 130603B (which is based on a single detection and thus poorly constrained), Ascenzi et al. (2019) found a range of $M_{ej} \approx 0.05$–$0.1 \ M_\odot$ using detailed modeling of the few *detected* short GRB candidate kilonovae and the K17 models. We derive overall stronger constraints using a newer, larger sample of upper limits and the K17 models, finding $M_{ej} \lesssim 0.05 \ M_\odot$ for six bursts (Table 1).

4.4. Model-dependent Constraints on Kilonova Ejecta Masses

Our method of translating limits to allowed ejecta masses and velocities demonstrates a high dependence on the assumed model. Indeed, for a given upper limit, the ejecta mass constraints can vary on the order of $0.1 \ M_\odot$ between the K17 and M19 analyses (see Table 1). While we analyze a larger number of bursts on the M19 grid, this is entirely because of the larger parameter space enabled by a purely analytic versus numerical calculation of kilonova light curves. Overall, while the analytic M19 light curves enable us to have significantly finer sampling and more dynamic range in M_{ej}–V_{ej}, we obtain *less* stringent constraints for each given burst than with the K17 models. We attribute this discrepancy to differences in the opacity between K17 and M19.

In the former, opacity is calculated numerically from the ionization state and abundance distribution of r-process species whose bound–bound transitions dominate the kilonova spectrum (in the Sedona code, as in Kasen et al. 2006, 2013, 2017). Alternatively, M19 assumes that the escaping spectrum resembles a blackbody with a constant effective opacity. Thus, the luminosity in each band around and after peak light where our observations are most constraining depends on the effective temperature of the ejecta and thus the equipartition of luminosity into each band. As nearly all of our observations are far into the Wien tail of the rest-frame kilonova spectrum, even small discrepancies in temperature can lead to large differences in peak magnitude. Moreover, while K17 performs a full radiative transfer calculation through each layer of the ejecta, incorporating deposition of radioactive energy and opacity (notably, the "blue" kilonova was reproduced assuming a steeply varying radial density and lanthanide abundance profile; Kasen et al. 2017; Kilpatrick et al. 2017), the effects from emission produced in the optically thin layers are not considered in M19. Table 1 shows the differences between constraints of the same limits on the M19 grid, which employ opacities that vary with the changing composition and ejecta expansion, and the K17 grid, which uses opacities based on a full numerical calculation. The discrepancy in allowed ejecta masses and velocities at similar Y_e values reinforces the model-dependent nature of our results. In addition to model dependencies, we note that five bursts in our sample (Table 1) have unknown redshifts. However, the majority of these bursts have weak ejecta mass constraints ($M_{ej} \lesssim 0.1 \ M_\odot$) and do not affect our strongest conclusions.

An outstanding theoretical challenge is determining the mechanism that produces the fast ($v \sim 0.2$–$0.3c$), blue ($Y_e \gtrsim 0.25$) ejecta needed to replicate the early ($\delta t \lesssim 1$ day), luminous, optical peak of AT 2017gfo (see summary in Metzger 2017; Banerjee et al. 2020). It is unclear how these emission mechanisms can match the bright, optical detections of kilonova candidates given the timescales required for neutrinos to raise the electron fraction in the dynamical ejecta (Fernández et al. 2019). Previous studies have examined potential additional energy sources but have been unable to account for the luminosity peak at timescales greater than a few hours (Metzger et al. 2015; Kasliwal et al. 2017a; Piro & Kollmeier 2018). Magnetic fields of the remnant NS or from the accretion disk may play a role in increasing the velocity of high-Y_e ejecta (Metzger et al. 2018; Christie et al. 2019; Fernández et al. 2019). Future observations will enhance our understanding of the early, bright optical peak of AT 2017gfo in connection to short GRB kilonovae.

5. Discussion

5.1. Implications for r-process Production

One of the most fundamental questions regarding BNS mergers is the fraction of cosmic *r*-process production for which they are responsible, in part a function of how much material they eject into the interstellar or intergalactic medium. Studies of the kilonovae associated with short GRBs are crucial because they enable an estimate of the average *r*-process yield per event. In turn, this can indicate whether BNS mergers, rather than collapsars (Siegel et al. 2019) or other phenomena, created the majority of *r*-process elements in the universe. Combined with the rates of mergers from either GW or GRB observations, and the timescale over which the mass is assembled, one can estimate the total contribution of mergers to *r*-process enrichment in the universe (e.g., Shen et al. 2015; Rosswog et al. 2018).

Initially, the relatively high yields inferred from AT 2017gfo, coupled with the volumetric merger event rates inferred from GW170817 of $R_{BNS} = 1540^{+3200}_{-1220}$ Gpc^{-3} yr^{-1} (90% confidence; Abbott et al. 2017c), suggested that if all kilonovae are similar to this event, the observed *r*-process abundance in the Galaxy would be overproduced (Kasen et al. 2017). However, the most recent results from the O3a run of LIGO/Virgo find a lower median event rate of $R_{BNS} = 320^{+490}_{-240}$ Gpc^{-3} yr^{-1} (90% confidence; Abbott et al. 2021). This rate is still broadly consistent with estimates obtained from population synthesis (Kim et al. 2015) and from short GRBs (Fong et al. 2015), implying that average yields close to that of AT 2017gfo may in fact be needed to explain all *r*-process production.

If BNS mergers account for all *r*-process material, this sets a constraint on a combination of the required event rates and ejected masses. In practice, this depends on the abundances of *r*-process elements in the ejecta, rather than the total mass of the material ejected. Indeed, Rosswog et al. (2018) demonstrate that the required event rate is comparatively higher if BNS mergers create all *r*-process elements (e.g., both light and heavy *r*-process elements), while the required event rate is lower if BNS mergers only produce elements beyond atomic mass numbers of $A > 130$ (the second *r*-process peak). The lower atomic mass, first-peak *r*-process elements are best probed by the blue kilonova component constraints.

Our large observational catalog provides a far more extensive investigation of the ejecta masses than has previously been possible, and it divides the inferred ejecta mass constraints by component. While the upper limits of many short GRBs in our catalog constrain ejecta masses significantly higher than those inferred for AT 2017gfo (Figure 4), there are a handful of events for which we can rule out component masses similar to estimates of this event (see also Ascenzi et al. 2019). However, we have also shown that the exact values of these parameters are still dependent on the choice of model (Table 1). For the extremely blue component, the inferred limits reach low ejecta masses of $M_{ej} \lesssim 0.03\,M_{\odot}$ for six (four) events in our sample under the K17 (M19) model. If the nondetections of kilonovae in a large fraction of our population are taken to be indicative of lower *r*-process yields in some systems, then other (unobserved) events must have significantly higher *r*-process yields for BNS mergers to be the sole site of *r*-process nucleosynthesis in the universe. A final consideration is that a significant fraction of short GRBs (and by extension BNS systems) occur at moderate distances (several kiloparsecs) from

their hosts (Church et al. 2011; Fong & Berger 2013). Thus, it is likely that not all *r*-process elements produced in BNS mergers become available for subsequent incorporation into stars. Nevertheless, this catalog motivates future studies that incorporate these factors, as well as a reexamination of our search strategies for kilonovae following short GRBs.

5.2. Short GRB Kilonovae in the Context of Current Observational Capabilities

Among our comprehensive sample of 85 short GRBs, we find that only a small fraction of upper limits can place meaningful constraints on kilonova models or the viable M_{ej}–V_{ej} parameter space. To represent where our limits fall with respect to expectations for realistic kilonova emission and current observational capabilities, we compare our catalog of limits to the light curves of AT 2017gfo and the NSBH model of Kawaguchi et al. (2020b). In Figure 5 we plot the *riJK*-band light curves of AT 2017gfo and the NSBH model scaled to $z = 0.2$, $z = 0.3$, and $z = 0.5$ (roughly the median detected short GRB redshift), accounting for redshift effects in choosing the relevant model.

Figure 5 shows the sheer number of optical (*r*- and *i*-band) upper limits at $\delta t \lesssim 2$ days, which dwarfs the number of deep, NIR observations on similar timescales. However, only 7.9% of optical (*griz* bands) upper limits are deep enough and on the relevant timescales to detect a nearby ($z \lesssim 0.3$) AT 2017gfo-like kilonova (Figure 5), with the NSBH model faring similarly. Kilonovae have the potential to exhibit redder colors and peak on longer timescales than afterglows, motivating past searches in the NIR bands on $\delta t \gtrsim 0.5$ days. However, only 1.7% of NIR (*JHK* bands) upper limits are sufficient to detect the kilonovae of low-redshift ($z \lesssim 0.3$) bursts. More broadly, none of the ∼100 *ground-based* NIR observations in our sample uncovered kilonova emission, and in only one case does a ground-based NIR observation probe lower luminosities than AT 2017gfo (GRB 160821B; $z = 0.1616$; Troja et al. 2019). Instead, all remaining NIR observations that detected or placed meaningful constraints on kilonova emission involved HST, which has uncovered kilonova candidates to $z \lesssim 0.6$ (Fox et al. 2005; Berger et al. 2013; Tanvir et al. 2013a; Lamb et al. 2019; Troja et al. 2019; Fong et al. 2021).

Ground-based optical observations have played a comparatively larger role in detecting kilonovae in bluer bands (e.g., GRB 050709; Hjorth et al. 2005a; Covino et al. 2006, GRB 060614; Della Valle et al. 2006, GRB 150101B; Fong et al. 2016, and GRB 160821B; Kasliwal et al. 2017b; Lamb et al. 2019; Troja et al. 2019), although the timing of constraining observations must be finely tuned given the early and bright optical afterglow. Comparing the AT 2017gfo and NSBH kilonova model light curves to the depths of targeted, deep, ground- and space-based observations, it is clear that space-based capabilities are required to detect the "average" short GRB at $z = 0.5$.

5.3. Future Short GRB Kilonova Observations

Motivated by the poor constraining power of most observations in our catalog and the established diversity of kilonovae, we next consider if and how current observing strategies could be adjusted to uncover or place constraints on kilonova emission following short GRBs. In doing this, we also consider the limits of observational resources. Given the precise
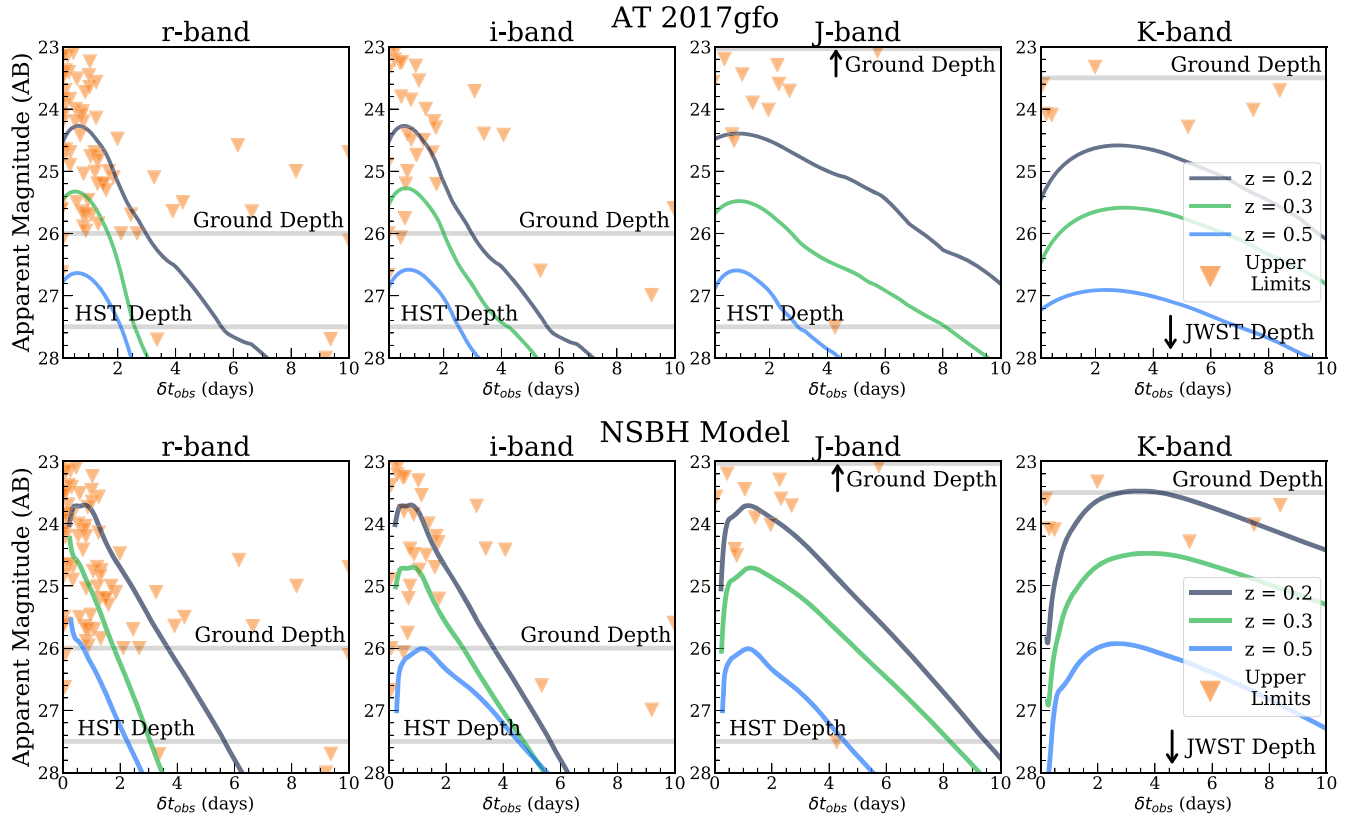
Figure 5. Observability of an AT 2017gfo-like (top) and NSBH (bottom; Kawaguchi et al. 2020b) kilonova shifted to $z = 0.2$, $z = 0.3$, and $z = 0.5$, the approximate median of the short GRB redshift distribution, in two optical (ri) and two NIR (JK) bands. In calculating light curves we account for redshift effects on time and observed band. We overlay historical upper limits as orange triangles and the depths of typical ground- and space-based telescopes as gray bars. In the optical, where ground-based telescopes are more powerful, future nearby ($z \lesssim 0.3$) kilonovae comparable to AT 2017gfo or the NSBH model will be detectable from the ground at $\delta t \lesssim 4$ days. In the NIR, space-based follow-up is necessary to detect kilonovae even at optimistic short GRB distances.

localizations of short GRBs (as compared to GW events), targeted searches on timescales ranging from ~hours to several days in a variety of filters are possible. However, given the relatively brighter, on-axis afterglows of short GRBs, optical kilonova searches are effectively limited to $\delta t \gtrsim 1$ day. For detections at early times, a determination of the true kilonova contribution would require nontrivial modeling of the bright afterglow, necessitating well-sampled, multiwavelength observations (e.g., GRB 160821B; Lamb et al. 2019).

In this vein, we investigate how the median expected magnitude of AT 2017gfo and kilonova models evolve with δt and redshift. We consider the NSBH and infinite-lifetime NS remnant previously mentioned in our comparative analysis (Kasen et al. 2015; Villar et al. 2017; Kawaguchi et al. 2020b). In addition, we include a magnetar-boosted model invoked by Fong et al. (2021) to explain the late-time ($\delta t_{rest} \approx 2.3$ days) infrared detections of GRB 200522A that were ≈ 10 times the luminosity of AT 2017gfo (but see also O'Connor et al. 2021 for an alternative interpretation). A magnetar kilonova model has also been invoked to explain the anomalously bright detections of GRB 050724A and GRB 070714B (Gao et al. 2017). Though the optimistic infinite-lifetime NS remnant and magnetar-boosted kilonovae are expected for a low percentage of cases (Margalit & Metzger 2019), their frequency has yet to be determined observationally (Schroeder et al. 2020). Thus, probing the luminosities of optimistic models will uniquely enhance our knowledge of the rates of these scenarios.

For each model in the $grizJK$ bands, we determine the median expected magnitude within 1-day bins for $\delta t \lesssim 6$ days

at 12 fixed redshifts equally spaced in the range $0 \lesssim z \lesssim 0.6$. We account for all redshift effects on time and approximate the light curves to the nearest rest-frame band. In Figure 6, we show the temporal evolution of each model as a function of redshift in the optical (r band) and NIR (J band). We show the same analysis applied to the $gizK$ bands in the Appendix (Figure A1). We also compare the temporal behavior to the depths of targeted searches for kilonova emission. For ground-based searches (solid lines) we compare to limiting magnitudes $m = 26$ mag and $m = 23$ mag in the gri and zJK bands, respectively, based on a typical 30-minute exposure time in good conditions (seeing less than ~0.75″ and air mass below ~1.2) with an 8 m class telescope. Finally, to highlight how this parameter space is sampled by short GRB observations, we plot all upper limits of short GRBs with known redshift. We divide them into limits that reached the appropriate depth to rule out the model (circles) and those that were too shallow and did not reach the appropriate depth (crosses). The color of the limit markers corresponds to the difference in magnitude between the depth of the observation and the median depth of the model in that bin (ΔMagnitude = $m_{obs} - m_{model}$, where positive values indicate sufficient depths to rule out the model; Figure 6).

In the optical bands, AT 2017gfo-like and NSBH model-like kilonovae are only detectable by ground-based telescopes on short timescales ($\delta t \lesssim 2$ days) out to redshifts of $z \approx 0.4$, while ground-based NIR observations cannot play a significant role. The exception across all bands and models is for very nearby $z \lesssim 0.15$ short GRBs, which are detectable on longer timescales
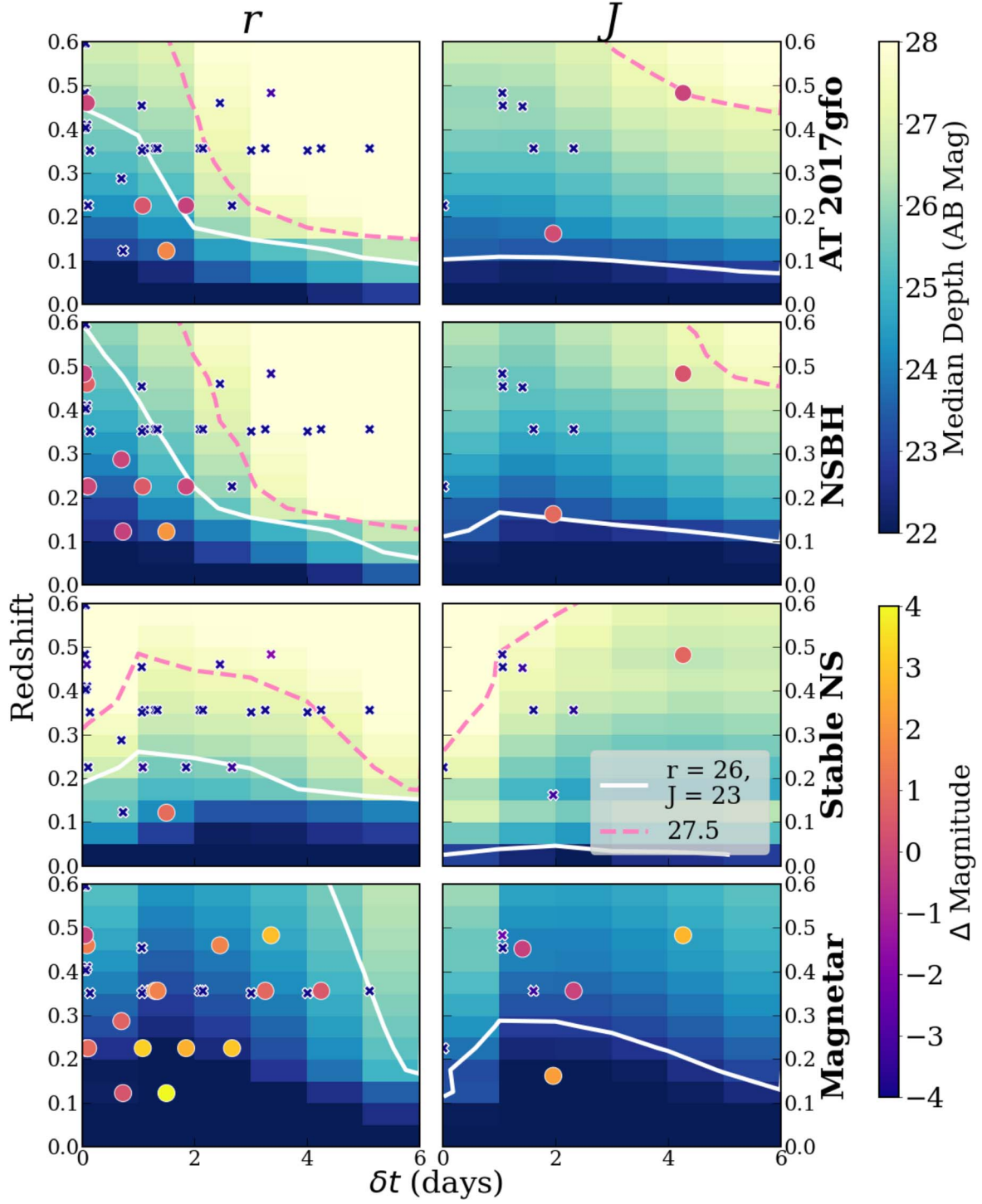
Figure 6. The median expected apparent magnitudes of AT 2017gfo light curves and three kilonova models (rows) in the observed r (left column) and J bands (right column) found within 1-day bins at 12 equally spaced redshifts in the range $0 < z < 0.6$. The median depths correspond to the color bar in the upper right corner and account for redshift effects on time and observed wavelength. We also plot two contours showing the limits of ground-based ($m = 26$ mag in r band and $m = 23$ mag in J band; while solid lines) and space-based telescopes ($m = 27.5$ mag; pink dashed lines). The space below these contours is considered observationally achievable by the respective facilities. We also plot past upper limits of short GRBs with known redshift, dividing them into limits that reached the appropriate depth to rule out the model (circles) and those that were too shallow and did not reach the appropriate depth (crosses). The color of each limit marker corresponds to the difference in magnitude between the observation and the median depth of the model (ΔMagnitude $= m_{\mathrm{obs}} - m_{\mathrm{model}}$) and correspond to the color bar in the lower right corner. The majority of observations of low-redshift bursts are taken in the r band, despite the NIR light curves' longer timescale of observability.

to $\delta t \approx 5$ days. Overlaying our short GRB catalog also highlights the regions of parameter space that are infrequently sampled but observationally achievable. For example, though the very low redshift ($z < 0.2$) portion of the r-band grids is

somewhat populated, few NIR observations exist for these rare, nearby bursts, despite the ground-based observability of typical kilonovae. As NIR light curves (and NSBH models in particular) benefit from the slower time evolution of the

lanthanide-rich, higher-opacity ejecta, observers have >5 days to obtain multiple, deep ground-based follow-up of the most nearby ($z < 0.2$) bursts, potentially supplying critical color information. Deep ($m > 24.5$), ground-based optical observations of $z \approx 0.3$–0.4 bursts at $\delta t \approx 1$–2 days can play a role in uncovering or placing meaningful constraints on further AT 2017gfo-like and NSBH model-like kilonovae.

Naturally, optical and NIR space-based imaging (one to two orbits of HST reaching $m = 27.5$ mag; dashed pink lines) significantly widens the achievable parameter space to higher redshifts and longer timescales, when afterglow contamination is not an issue. Figure 6 highlights the necessity of space-based facilities like HST and the upcoming JWST.

Finally, when considering optimistic but rarer models, such as the magnetar-boosted kilonova, ground-based optical telescopes can play a singular role in ruling out this model to $z \approx 0.6$ and beyond at $\delta t \lesssim 4$ days. Ground-based NIR observations can also play a crucial role in supplying color information to $z \approx 0.3$. Combined with the intriguing counterpart of GRB 200522A (Fong et al. 2021), we find motivation for late ($\delta t \gtrsim 2$ days), deep ($m > 25$ mag) ground-based optical follow-up of short GRBs to fully and effectively explore the range of kilonova emission.

In summary, our investigation of the future observability of short GRB kilonovae suggests that the best detection strategies are to (i) continue to conduct deep, ground-based follow-up at $\delta t = 1$–2 days, as this allows us to probe diverse kilonova at a wide range of distances while avoiding significant afterglow contamination; (ii) observe low-redshift bursts in the NIR bands to $\delta t \approx 8$ days, a region of the parameter space that is currently unexplored by observations; and (iii) use NIR space-based telescopes such as HST and JWST to follow up short GRBs at $z \lesssim 1$ for up to ~ 10 days post-burst (Figure 5). This final point will require continued rapid-response capabilities of space-based missions.

6. Conclusion

We present a new catalog of 261 observations of 85 short GRBs (39 with known redshifts; Table A1), the largest sample considered to date. This catalog includes over 50 unpublished upper limits of 23 short GRBs. Our analysis definitively establishes the wide diversity of kilonovae, confirming and expanding on the findings of previous works (Gompertz et al. 2018; Ascenzi et al. 2019; Rossi et al. 2020b). Our emphasis on deep upper limits allows us to explore a portion of the short GRB observational catalog that has not been the focus of previous short GRB kilonova studies. Beyond this, we constrain the ejecta masses and velocities of 14 short GRB kilonovae and inform future kilonova-targeted observing strategies. While only a small fraction of the existing catalog places constraints probed by the parameter space of known kilonovae, the large data set is broadly informative for a diverse set of current (and future) kilonova models and observations. Our main conclusions are as follows:

1. We find upper limits of 11.8% and 15.3% of short GRBs (including 20.5% and 23.1% of bursts with known redshift) in our catalog that probe luminosities deeper than those of AT 2017gfo or a fiducial, pole-on NSBH model, respectively. Seventy-five percent of upper limits deeper than AT 2017gfo are in the rest-frame optical,

highlighting the sensitivity of the catalog to bluer kilonovae. These limits were derived from observations at 0.1 days $\lesssim \delta t \lesssim 4$ days, reinforcing the need for continued follow-up of well-localized short GRBs within a few days of discovery.

2. We consider additional models, including that of an indefinitely stable NS remnant kilonova and a GW190425-like kilonova. We find that approximately a quarter of upper limits in the short GRB sample probe luminosities lower than the optimistic GW190425-like kilonova model.

3. In general, the kilonova candidates detected from short GRBs are on the upper end of the luminosity distribution, consistent with expectations for the magnitude-limited sample we have constructed.

4. While we could not place numerical constraints on V_{ej}, we can constrain the blue component ejecta masses ($X_{lan} = 10^{-4}$) for nine bursts to $M_{ej} < 0.01$–0.1 $M_\odot$. For an extremely blue component ejecta mass ($X_{lan} = 10^{-9}$), the limits also constrain $M_{ej} < 0.01$–0.1 $M_\odot$ for 12 bursts. We find that precise values are model dependent.

5. Despite the sustained NIR-band luminosity of kilonovae like the NSBH merger model, the timescales of past ground-based NIR observations are typically too early to rule out these kilonova models. Our analysis finds motivation for deep ($m > 23$) observations at $\gtrsim 2$ days of nearby ($z \lesssim 0.2$) bursts to detect potential NSBH kilonovae.

6. Despite the sustained optical brightness of the infinite-lifetime NS remnant model, few current observations are on the appropriate timescales to probe this model. Future optical follow-up should concentrate on timescales of $\gtrsim 2$–6 days when such models reach their peak.

7. Optical observations generally probe realistic kilonova luminosity functions, but there are almost no low-redshift short GRB NIR observations, despite their detectability with current instruments. In addition, ground-based optical telescopes are capable of probing diverse kilonova outcomes for bursts over a range of redshifts, while future space-based facilities will extend the reach of detecting kilonovae to $z \approx 1$, highlighting the importance of rapid-response observations on current and future missions.

The past 15 yr of well-localized short GRBs discovered by Swift and concerted follow-up of their afterglows provide a unique opportunity to recast deep limits in terms of known kilonovae and a diverse set of optical and NIR models. Positively identifying these transients as kilonovae is difficult at all distances given their faintness and rapid evolution compared to other transients. While detecting kilonovae following short GRBs pushes the limits of current observatories, searches remain a worthwhile endeavor in the current era of GRB discovery and localization. In particular, it is imperative to maintain broad and flexible search strategies (in terms of timescales, depths, and colors) to detect or meaningfully constrain kilonova emission across the diversity of potential outcomes. Although current and future transient surveys may be capable of finding $z > 0.1$ kilonovae on their own (Scolnic et al. 2018; McBrien et al. 2020), the only promising method to positively identify them is by association with short GRBs or GW events. Historically, HST has played an invaluable role in identifying short GRB kilonova candidates and placing deep limits on emission. Moving forward,

Appendix A
Supplementary Information

The appendix includes the full catalog of short GRB kilonova observations using in this work (Table A1) as well as an extended version of Figure 6 (Figure A1).

Table A1
Catalog of Short GRB Kilonova Observations

GRB	z	Telescope/Instrument	δt (days)	Filter	Magnitude (AB mag)	Error (AB mag)	νL_ν (erg s^{-1})	Reference
050509B	0.225	WIYN/OPTIC	0.09	r	>24.2		<5.5×10^{41}	2
		WIYN/OPTIC	0.10	r	>23.8		<7.8×10^{41}	2
		WIYN/OPTIC	0.10	r	>23.9		<7.7×10^{41}	2
		WIYN/OPTIC	0.11	r	>24.1		<6.1×10^{41}	2
		Keck I/LRIS	1.08	R	>25.6		<1.5×10^{41}	3
		VLT/FORS	1.85	R	>25.1		<2.4×10^{41}	4
		6.0BTA/SCORPIO	2.67	R	>26.0		<1.1×10^{41}	5
050709[a]	0.161	Danish tel./DFOSC	1.41	R	23.0	0.1	8.1×10^{41}	6
		VLT/FORS2	2.47	R	24.0	0.1	3.2×10^{41}	7
		Danish tel./DFOSC	2.50	R	23.7	0.2	4.1×10^{41}	6
		VLT/FORS1	4.36	V	>25.0		<1.6×10^{41}	7
		HST/ACS	5.60	F814W	25.1	0.1	1.2×10^{41}	8
		HST/ACS	9.80	F814W	25.8	0.1	6.0×10^{41}	8
050724A[a]	0.257	Magellan/Baade/PANIC	1.45	K	>22.1		<1.5×10^{42}	9
		VLT/FORS1	1.45	I	22.8	0.1	2.2×10^{42}	10
		Swope 40 in.	1.53	I	>21.5		<7.0×10^{41}	9
		VLT/FORS1	1.46	R	22.6	0.1	3.3×10^{42}	10
		VLT/FORS1	3.46	I	25.1	0.3	2.5×10^{41}	10
050813	0.72	CAHA/CAFOS	0.55	I	>23.2		<1.6×10^{43}	11
		CAHA/CAFOS	0.59	R	>23.5		<1.6×10^{43}	11

Table A1
(Continued)

GRB	z	Telescope/Instrument	δt (days)	Filter	Magnitude (AB mag)	Error (AB mag)	νL_ν (erg s^{-1})	Reference
050906[b]	[c]	VLT/FORS2	0.89	R	>26.0		<7.1 × 10^{41}	12
051210	[c]	Magellan/Clay/LDSS3	0.81	r	>25.9		9.3 × 10^{42}	13
051221A	0.546	Gemini-N/GMOS	6.16	r	>24.6		<3.0 × 10^{42}	14
060121	[c]	WIYN	1.40	R	24.9	0.2	1.9 × 10^{42}	15
060313	[c]	Gemini-S/GMOS	10.0	r	>24.7		<2.2 × 10^{42}	13
060502B	0.287	Gemini-N/GMOS	0.70	R	>24.3		<8.9 × 10^{41}	16
060614[a]	0.125	VLT/FORS1	3.86	I	24.2	0.6	1.3 × 10^{41}	17
		VLT/FORS1	3.87	R	25.5	0.3	4.6 × 10^{40}	17
		VLT/FORS1	4.85	R	25.1	0.3	6.6 × 10^{40}	17
		VLT/FORS1	6.74	R	25.5	0.3	4.6 × 10^{40}	17
		VLT/FORS1	7.84	I	25.1	0.4	5.7 × 10^{40}	17
061201	0.111	VLT/FORS2	0.36	I	22.8	0.1	3.6 × 10^{41}	18
		VLT/FORS2	0.38	R	23.2	0.1	3.0 × 10^{41}	18
		VLT/FORS2	1.38	I	>24.0		<1.2 × 10^{41}	18
		VLT/FORS2	3.39	I	>24.4		<8.0 × 10^{40}	18
061217[b]	0.827	Magellan/Clay/LDSS3	0.12	r	>23.1		<3.2 × 10^{42}	13
070406[b]	[c]	NOT/ALFSOC	1.02	R	>23.6		<5.9 × 10^{42}	19
070429B	0.902	Gemini-S/GMOS	0.20	R	>24.7		<9.8 × 10^{42}	20
		Blanco/ISPI	1.13	J	>22.4		<4.0 × 10^{43}	21
070707	[c]	VLT/ISAAC	2.54	J	>24.5		<1.4 × 10^{42}	22
070714B[a]	0.923	TNG/NICS	1.00	J	>21.5		<9.3 × 10^{43}	23
		TNG/NICS	1.00	K	22.8	0.3	1.7 × 10^{43}	23
		WHT	1.03	R	23.7	0.3	2.6 × 10^{43}	24
		Keck I/LRIS	4.40	R	25.7	0.3	4.1 × 10^{42}	25
070724A	0.457	Gemini-N/GMOS	0.10	g	>23.5		<7.0 × 10^{42}	26
070729	0.8	ESO/MPG/GROND	0.35	R	>24.7		<7.0 × 10^{42}	27
		ESO/MPG/GROND	0.35	J	>22.7		<2.3 × 10^{43}	27
070809[a]	0.473	Keck I/LRIS	0.47	g	25.1	0.2	1.8 × 10^{42}	28
		Keck I/LRIS	0.47	R	23.9	0.3	4.2 × 10^{42}	28
		Keck I/LRIS	1.46	g	>25.4		<1.4 × 10^{42}	28
		Keck I/LRIS	1.46	R	24.8	0.3	1.8 × 10^{42}	28
071112B[b]	[c]	Magellan/Clay/LDSS3	0.26	r	>23.1		<9.3 × 10^{42}	29
		ESO/MPG/GROND	0.40	J	>21.6		<2.0 × 10^{42}	27
080503	[c]	Gemini-N/GMOS	0.04	r	>25.6		<9.7 × 10^{41}	30
		Gemini-N/GMOS	0.05	g	26.5	0.2	5.5 × 10^{41}	30
		Keck I/LRIS	0.05	R	>25.6		<9.9 × 10^{41}	30
		Gemini-N/GMOS	0.06	r	>26.6		<3.8 × 10^{41}	30
		Gemini-N/GMOS	0.08	i	>26.7		<3.0 × 10^{41}	30
		Gemini-N/GMOS	0.09	z	>25.9		<5.2 × 10^{41}	30
		Gemini-N/GMOS	1.08	r	25.3	0.1	1.3 × 10^{42}	30
		Gemini-N/GMOS	1.98	r	25.5	0.2	1.1 × 10^{42}	30
		Gemini-N/GMOS	2.09	g	26.3	0.3	7.1 × 10^{41}	30
		Gemini-N/GMOS	3.08	r	25.7	0.3	1.1 × 10^{42}	30
		Gemini-N/GMOS	4.05	r	26.1	0.2	7.1 × 10^{41}	30
		HST/WFPC2	5.36	F606W	26.9	0.2	3.0 × 10^{41}	30
080905A	0.122	NOT/ALFSOC	0.35	R	24.3	0.5	1.4 × 10^{41}	31
		VLT/FORS2	0.60	R	24.5	0.3	1.1 × 10^{41}	31
		ESO/MPG/GROND	0.73	r	>22.5		<8.7 × 10^{41}	27
		VLT/FORS	1.50	R	>25.2		<5.7 × 10^{40}	31
090305[b]	[c]	Gemini-S/GMOS	0.90	r	>25.7		<3.7 × 10^{40}	32
090515	0.403	Gemini-N/GMOS	0.07	r	26.3	0.1	3.1 × 10^{41}	33
		Gemini-N/GMOS	1.04	r	26.5	0.3	2.6 × 10^{41}	33
090621B	[c]	RTT150/TFOSC	0.03	r	>23.2		<8.9 × 10^{42}	34
091109B	[c]	VLT/FORS2	0.25	R	24.3	0.1	3.2 × 10^{42}	32
		VLT/HAWK-I	0.30	K	>24.1		<1.1 × 10^{42}	32
		VLT/HAWK-I	0.35	J	>22.9		<5.7 × 10^{42}	32
		VLT/FORS2	0.43	R	24.6	0.2	2.4 × 10^{42}	32
		VLT/FORS2	1.32	R	>25.8		<8.0 × 10^{41}	32
100206	0.407	ESO/MPG/GROND	0.49	i	>23.3		<4.0 × 10^{42}	27

Table A1
(Continued)

GRB	z	Telescope/Instrument	δt (days)	Filter	Magnitude (AB mag)	Error (AB mag)	νL_ν (erg s^{-1})	Reference
		Gemini-N/GMOS	0.65	i	>25.8		<4.3 × 10^{41}	35
100625A	0.452	ESO/MPG/GROND	0.51	g	>23.6		<6.0 × 10^{42}	27
		Magellan/PANIC	1.41	J	>23.9		<1.9 × 10^{42}	27
100628A	[c]	Gemini-N/GMOS	0.05	i	>24.1		<3.9 × 10^{42}	36
		Magellan/PANIC	0.74	J	>22.1		<1.3 × 10^{43}	36
100702A	[c]	ESO/MPG/GROND	0.07	r'	>23.2		<9.1 × 10^{42}	27
101219A	0.718	Gemini-S/GMOS	0.04	i	>24.9		<3.5 × 10^{42}	37
		Magellan/FourStar	0.05	J	>23.6		<7.9 × 10^{42}	37
110420B[b]	[c]	Magellan/IMACS	0.44	r	>23.5		<6.5 × 10^{42}	36
111020A	[c]	Gemini-S/GMOS	0.74	i	>24.4		<2.4 × 10^{42}	38
		VLT/HAWK-I	0.77	J	>24.5		<2.4 × 10^{42}	32
111117A	2.211	GTC/OSIRIS	0.34	r	>24.9		<7.1 × 10^{43}	39
		Gemini-S/GMOS	0.57	r	>25.5		<4.1 × 10^{43}	40
120521A	[c]	ESO/MPG/GROND	0.78	r	>24.0		<4.1 × 10^{42}	41
120817B	[c]	LCO/duPont/WFCCD	1.00	R	>23.5		<7.0 × 10^{42}	42
130313A	[c]	Gemini-S/GMOS	0.62	i	>25.7		<7.3 × 10^{41}	1
		NOT/ALFSOC	0.42	i	>23.4		<6.1 × 10^{42}	43
		TNG	0.56	r	>25.0		<1.7 × 10^{42}	44
130515A	[c]	Gemini-S/GMOS	0.03	r	>23.5		<6.5 × 10^{42}	45
130603B[a]	0.356	HST/ACS	9.37	F606W	>27.7		<7.7 × 10^{40}	46, 47
		HST/WFC3	9.49	F160W	25.8	0.2	1.4 × 10^{41}	46, 47
130716A	[c]	Gemini-N/GMOS	0.81	r	>25.0		<9.7 × 10^{41}	36
130822A	0.154	Gemini-N/GMOS	0.88	i	>24.5		<1.5 × 10^{41}	48
		UKIRT/WFCAM	5.69	H	>22.8		<3.4 × 10^{41}	1
		UKIRT/WFCAM	6.69	J	>22.0		<9.4 × 10^{41}	1
130912A	[c]	WHT/ACAM	0.84	g	>24.1		<2.2 × 10^{42}	49
		WHT/LIRIS	0.88	J	>22.1		<1.3 × 10^{43}	1
		HJT/RATIR	1.04	r	>23.3		<8.5 × 10^{42}	50
		HJT/RATIR	1.04	i	>23.3		<6.5 × 10^{42}	50
		HJT/RATIR	1.04	J	>22.1		<1.3 × 10^{43}	50
		UKIRT/WFCAM	1.2	J	>22.3		<2.1 × 10^{43}	1
		UKIRT/WFCAM	1.2	H	>22.0		<1.1 × 10^{43}	1
		WHT/LIRIS	7.71	J	>22.8		<6.8 × 10^{42}	1
		Magellan/FourStar	11.92	J	>23.7		<2.9 × 10^{42}	1
131004A	0.717	HJT/RATIR	0.30	r	>23.4		<1.7 × 10^{43}	51
		HJT/RATIR	0.30	i	>23.2		<1.7 × 10^{43}	51
		HJT/RATIR	0.30	Z	>22.7		<2.3 × 10^{43}	51
		HJT/RATIR	0.30	Y	>22.2		<3.2 × 10^{43}	51
		HJT/RATIR	0.30	J	>22.5		<2.0 × 10^{43}	51
		HJT/RATIR	0.30	H	>22.5		<1.5 × 10^{43}	51
131224A[b,d]	[c]	GTC	1.11	z	>23.1		<3.1 × 10^{42}	52
140402A[b]	[c]	Magellan/Baade/IMACS	1.21	r	>25.0		<1.7 × 10^{42}	36
140516	[c]	NOT/ALFSOC	0.08	R	>24.7		<2.3 × 10^{42}	53
		Subaru/IRCS+AO188	0.48	K'	>24.1		<1.1 × 10^{42}	54
		Gemini-N/GMOS	0.52	i	>26.1		<5.2 × 10^{41}	36
		HJT/RATIR	0.54	J	>22.0		<1.4 × 10^{42}	55
140606A[b]	[c]	BTA	0.39	V	>24.2		<4.5 × 10^{42}	52
		BTA	0.43	R_c	>26.0		<7.0 × 10^{41}	52
140619B[b,e]	[c]	Magellan/Baade/FourStar	1.48	J	>22.9		<6.1 × 10^{42}	36
140622A	0.959	GTC	0.78	r	>25.4		<4.6 × 10^{42}	52
140903A	0.351	MMT/MMTCam	7.53	r	>22.6		<6.8 × 10^{42}	1
		MMT/MMTCam	7.50	i	>22.9		<4.3 × 10^{42}	1
140930B	[c]	GTC	3.14	r	>24.5		<2.8 × 10^{42}	52
141212A	0.596	Gemini-N/GMOS	0.69	i	>25.2		<1.8 × 10^{42}	1
		Gemini-N/GMOS	1.75	i	>25.2		<1.8 × 10^{42}	1
150101B[a]	0.134	Magellan/Baade/IMACS	1.66	r	23.0	0.2	2.4 × 10^{42}	56
		Magellan/Baade/IMACS	2.63	r	23.5	0.3	5.2 × 10^{41}	56
		Gemini-S/GMOS	10.71	r	>24.2		<1.7 × 10^{41}	56
150120A	0.46	Gemini-N/GMOS	0.08	i	>26.0		<4.6 × 10^{41}	1
		Gemini-N/GMOS	0.08	r	>26.1		<5.1 × 10^{41}	1

Table A1
(Continued)

GRB	z	Telescope/Instrument	δt (days)	Filter	Magnitude (AB mag)	Error (AB mag)	νL_ν (erg s^{-1})	Reference
		Gemini-N/GMOS	0.13	z	>25.4		$<6.6 \times 10^{41}$	1
		Gemini-N/GMOS	2.16	r	>25.7		$<7.4 \times 10^{41}$	1
150423A	1.394	Magellan/IMACS	0.10	i	23.6	0.1	6.5×10^{43}	1
		WHT/ACAM	0.67	g	>25.2		$<2.3 \times 10^{43}$	57
		HJT/RATIR	1.06	r	>24.8		$<2.7 \times 10^{43}$	58
		HJT/RATIR	1.06	i	>24.7		$<2.2 \times 10^{43}$	58
		HJT/RATIR	1.06	z	>22.0		$<2.2 \times 10^{43}$	58
150424A	[c]	ESO/MPG/GROND	1.81	r'	23.1	0.1	5.5×10^{43}	59
		ESO/MPG/GROND	1.81	i'	23.0	0.1	4.7×10^{43}	59
		ESO/MPG/GROND	1.81	z'	22.6	0.1	5.7×10^{43}	59
		HST/WFC3	6.64	F606W	25.9	0.1	4.1×10^{42}	60
		HST/WFC3	6.68	F125W	25.3	0.1	3.7×10^{42}	60
		HST/WFC3	6.71	F160W	25.1	0.1	3.3×10^{42}	60
		HST/WFC3	9.23	F606W	26.9	0.1	1.6×10^{42}	60
		HST/WFC3	9.26	F125W	26.3	0.2	1.5×10^{42}	60
		HST/WFC3	9.30	F160W	25.8	0.1	1.8×10^{42}	60
150831A	[c]	ESO/MPG/GROND	0.53	g'	>24.5		$<3.6 \times 10^{42}$	61
		ESO/MPG/GROND	0.53	r'	>24.2		$<3.6 \times 10^{42}$	61
		ESO/MPG/GROND	0.53	i'	>23.8		$<4.2 \times 10^{42}$	61
		ESO/MPG/GROND	0.53	z'	>23.6		$<4.2 \times 10^{42}$	61
		ESO/MPG/GROND	0.53	J	>21.3		$<2.7 \times 10^{43}$	61
151228A[b]	[c]	GTC	1.14	i	>23.7		$<5.1 \times 10^{42}$	52
160303A	[c]	UKIRT/WFCAM	0.84	J	>22.0		$<1.4 \times 10^{43}$	1
		UKIRT/WFCAM	0.87	K	>22.0		$<7.7 \times 10^{42}$	1
		HJT/RATIR	0.87	r	>23.7		$<5.6 \times 10^{42}$	62
		HJT/RATIR	0.87	i	>23.9		$<4.0 \times 10^{42}$	62
		HJT/RATIR	0.87	Z	>22.4		$<1.3 \times 10^{43}$	62
		HJT/RATIR	0.87	Y	>21.8		$<2.1 \times 10^{43}$	62
		HJT/RATIR	0.87	J	>21.5		$<2.2 \times 10^{43}$	62
		HJT/RATIR	0.87	H	>21.4		$<1.8 \times 10^{43}$	62
		ESO/MPG/GROND	1.73	i'	>24.3		$<2.6 \times 10^{42}$	63
		ESO/MPG/GROND	1.73	z'	>24.4		$<2.0 \times 10^{42}$	63
		MMT/MMTCam	3.90	r	>25.6		$<9.5 \times 10^{41}$	1
		MMT/MMTCam	10.82	i	>24.5		$<2.2 \times 10^{42}$	1
160408A	[c]	Gemini-N/GMOS	0.05	r	24.8	0.1	2.1×10^{42}	1
		Gemini-N/GMOS	0.97	r	>25.5		$<1.1 \times 10^{42}$	1
160410A	1.717	UKIRT/WFCAM	1.06	J	>22.2		$<1.2 \times 10^{43}$	1
		UKIRT/WFCAM	1.09	K	>21.8		$<9.4 \times 10^{42}$	1
		NOT/ALFSOC	1.68	r	>25.0		$<1.7 \times 10^{42}$	64
160411A	[c]	Gemini-S/GMOS	0.34	i	23.3	0.2	6.5×10^{42}	1
		ESO/MPG/GROND	0.34	g'	>23.6		$<8.0 \times 10^{42}$	65
		ESO/MPG/GROND	0.34	r'	>23.8		$<5.0 \times 10^{42}$	65
		ESO/MPG/GROND	0.34	i'	>23.1		$<8.4 \times 10^{42}$	65
		ESO/MPG/GROND	0.34	z'	>22.9		$<8.2 \times 10^{42}$	65
		ESO/MPG/GROND	0.34	J	>21.3		$<2.7 \times 10^{43}$	65
		ESO/MPG/GROND	0.34	H	>20.8		$<3.2 \times 10^{43}$	65
160601A	[c]	DCT/LMI	1.60	r	>25.0		$<1.7 \times 10^{42}$	66
160612A[b]	[c]	UKIRT/WFCAM	2.69	J	>23.7		$<2.9 \times 10^{42}$	1
		UKIRT/WFCAM	5.74	J	>23.1		$<5.3 \times 10^{42}$	1
160624A	0.483	Gemini-N/GMOS	0.003	r	>25.5		$<1.0 \times 10^{42}$	67
		Gemini-N/GMOS	0.05	r	>24.8		$<1.9 \times 10^{42}$	1
		UKIRT/WFCAM	1.05	J	>23.4		$<3.4 \times 10^{42}$	1
		HST/ACS	3.36	F606W	>27.7		$<1.3 \times 10^{41}$	68, 1[g]
		HST/WFC3	4.27	F125W	>27.5		$<8.2 \times 10^{40}$	68, 1[g]
		HST/WFC3	4.33	F160W	>27.3		$<7.4 \times 10^{40}$	68, 1[g]
160821B[a]	0.1616	WHT/ACAM	1.06	r	23.8	0.1	3.8×10^{41}	69
		WHT/ACAM	1.08	z	23.6	0.2	3.1×10^{41}	69
		GTC/CIRCE	1.94	H	>23.8		$<1.5 \times 10^{41}$	70
		NOT/ALFOSC	1.95	r	24.8	0.1	1.5×10^{41}	69

Table A1
(Continued)

GRB	z	Telescope/Instrument	δt (days)	Filter	Magnitude (AB mag)	Error (AB mag)	νL_ν (erg s^{-1})	Reference
		GTC/CIRCE	1.96	J	>24.0		$<1.7 \times 10^{41}$	70
		NOT/ALFOSC	1.99	z	23.9	0.2	2.4×10^{41}	69
		GTC/OSIRIS	2.02	g	25.6	0.2	2.5×10^{41}	69
		GTC/OSIRIS	2.03	r	24.8	0.1	1.6×10^{41}	69
		GTC/OSIRIS	2.04	i	24.5	0.1	1.7×10^{41}	69
		GTC/OSIRIS	2.04	z	24.3	0.2	1.6×10^{40}	69
		HST/WFC3/UVIS	3.64	F606W	25.9	0.1	5.6×10^{40}	69
		HST/WFC3/IR	3.71	F160W	24.4	0.1	8.4×10^{40}	69
		HST/WFC3/IR	3.76	F110W	24.7	0.2	8.7×10^{40}	69
		GTC/OSIRIS	3.98	g	26.0	0.2	6.7×10^{40}	69
		GTC/OSIRIS	4.00	i	25.7	0.4	5.5×10^{40}	69
		GTC/OSIRIS	4.99	r	26.1	0.3	4.6×10^{42}	69
		GTC/OSIRIS	6.98	g	26.9	0.2	2.9×10^{40}	69
		GTC/OSIRIS	9.97	i	>25.6		$<6.0 \times 10^{40}$	69
		GTC/OSIRIS	10.00	g	>25.7		$<8.7 \times 10^{40}$	70
		HST/WFC3/UVIS	10.01	F606W	>26.1		$<4.6 \times 10^{40}$	69
		HST/WFC3/UVIS	10.40	F606W	27.7	0.1	1.1×10^{40}	69
		HST/WFC3/IR	10.46	F160W	26.6	0.2	1.2×10^{40}	69
		HST/WFC3/IR	10.53	F110W	26.7	0.2	1.4×10^{40}	69
161001A	0.891	ESO/MPG/GROND	0.12	J	>21.3		$<1.1 \times 10^{44}$	71
161104A	0.65	Gemini-S/GMOS	0.72	r	>25.4		$<1.2 \times 10^{42}$	72
170112A	[c]	UKIRT/WFCAM	1.17	J	>21.3		$<2.8 \times 10^{43}$	1
170127B	[c]	UKIRT/WFCAM	0.55	J	>21.0		$<3.5 \times 10^{43}$	1
		NOT/ALFSOC	0.19	r	>23.4		$<7.7 \times 10^{42}$	73
170428A	0.454	MMT/MMTCam	3.07	i	>23.7		$<3.6 \times 10^{42}$	1
		MMT/MMTCam	4.08	i	>24.4		$<1.9 \times 10^{42}$	1
		UKIRT/WFCAM	6.24	J	>22.0		$<1.1 \times 10^{42}$	1
		UKIRT/WFCAM	7.22	J	>22.7		$<5.9 \times 10^{42}$	1
		UKIRT/WFCAM	8.24	J	>22.7		$<5.9 \times 10^{42}$	1
		UKIRT/WFCAM	10.23	J	>22.5		$<7.1 \times 10^{42}$	1
170524A	[c]	UKIRT/WFCAM	0.79	K	>21.3		$<1.5 \times 10^{43}$	1
		UKIRT/WFCAM	2.76	K	>21.5		$<1.2 \times 10^{43}$	1
180418A	1.0[c]	Gemini-N/GMOS	4.80	r	>25.2		$<1.4 \times 10^{42}$	74
180715A[b]	[c]	UKIRT/WFCAM	0.52	J	>21.0		$<3.4 \times 10^{43}$	1
		Gemini-S/GMOS	0.54	r	>24.0		$<4.3 \times 10^{42}$	1
		UKIRT/WFCAM	1.51	J	>20.9		$<4.1 \times 10^{42}$	1
		UKIRT/WFCAM	2.58	J	>21.7		$<1.8 \times 10^{43}$	1
		UKIRT/WFCAM	7.54	J	>21.4		$<2.4 \times 10^{43}$	1
180718A[b,f]	[c]	Gemini-N/GMOS	1.50	r	>25.2		$<1.4 \times 10^{42}$	1
180727A	[c]	Magellan-Clay/LDSS3	1.66	i	>24.2		$<2.9 \times 10^{42}$	1
180805B	0.661	UKIRT/WFCAM	0.04	J	>22.3		$<2.1 \times 10^{43}$	1
		ESO/HAWK-I	0.70	J	>24.4		$<3.0 \times 10^{42}$	75
		NTT/EFOSC2	0.74	i	>25.0		$<2.8 \times 10^{42}$	76
		Magellan-Baade/IMACS	0.80	r	>24.2		$<7.1 \times 10^{42}$	1
		ESO/FORS2	0.82	R	>25.7		$<1.8 \times 10^{42}$	75
		UKIRT/WFCAM	1.04	J	>22.1		$<2.6 \times 10^{43}$	1
181123B	1.754	Keck I/MOSFIRE	0.43	J	>23.2		$<9.9 \times 10^{43}$	77
		MMT/MMIRS	2.27	J	>23.3		$<9.0 \times 10^{43}$	77
181126A	[c]	Gemini-N/GMOS	0.18	z	>25.3		$<8.9 \times 10^{41}$	78
		Keck I/MOSFIRE	0.18	K_s	>23.6		$<1.8 \times 10^{42}$	79
190427A[b]	[c]	NOT/ALFSOC	0.02	r	>23.5		$<6.9 \times 10^{42}$	80
191031D	[c]	MMT/Binospec	0.18	r	>24.1		$<4.1 \times 10^{42}$	1
		MMT/Binospec	0.18	z	>22.6		$<1.1 \times 10^{43}$	1
		HJT/RATIR	0.21	r	>22.8		$<1.4 \times 10^{42}$	81
		HJT/RATIR	0.21	i	>23.1		$<8.4 \times 10^{42}$	81
		MMT/Binospec	1.19	r	>24.4		$<3.1 \times 10^{42}$	1
		Gemini-N/GMOS	1.30	r	>24.8		$<2.0 \times 10^{42}$	82
200522A[a]	0.5537	Gemini/GMOS	3.12	r	26.0	0.4	8.8×10^{41}	68
		HST/WFC3	3.52	F125W	24.8	0.1	1.4×10^{42}	83

Table A1
(Continued)

GRB	z	Telescope/Instrument	δt (days)	Filter	Magnitude (AB mag)	Error (AB mag)	νL_ν (erg s^{-1})	Reference
		HST/WFC3	3.66	F160W	24.9	0.1	9.8×10^{41}	83
200623A[b,f]	[c]	LBT/LBC	2.11	r	>26.0		$<6.9 \times 10^{41}$	84
201221D	1.045	MMT/MMIRS	0.40	J	>23.1		$<3.1 \times 10^{43}$	1
		MMT/MMIRS	1.43	J	>23.3		$<2.6 \times 10^{43}$	1

Notes. This sample includes previously published (i) detections of kilonova candidates (marked with asterisks), (ii) deep ($m \gtrsim 21$ AB mag) upper limits, and (iii) low-luminosity ($\nu L_\nu \lesssim 5 \times 10^{41}$ erg s^{-1}) afterglow detections. Unless noted, all bursts are detected by Swift-BAT and Swift-XRT.
[a] Kilonova candidate.
[b] Burst does not have an X-ray afterglow found by Swift-XRT.
[c] Redshift unknown, $z = 0.5$ taken as fiducial value in analysis, except for GRB 180418A, which is assumed to be $z = 1.0$ (cf. Rouco Escorial et al. 2021).
[d] Burst detected by INTEGRAL-IBIS/ISGRI, not detected by Swift-BAT.
[e] Burst detected by Fermi-GBM, Fermi-LAT, and Suzaku-WAM, not detected by Swift-BAT.
[f] Limit applies to partial coverage of BAT localization.
[g] We present a separate analysis of observations published in (68), finding upper limits deeper by 0.2–0.3 mag.

References. (1) This work; (2) Bloom et al. 2006; (3) Cenko et al. 2005; (4) Hjorth et al. 2005a; (5) Castro-Tirado et al. 2005; (6) Hjorth et al. 2005b; (7) Covino et al. 2006; (8) Fox et al. 2005; (9) Berger et al. 2005; (10) Malesani et al. 2007a; (11) Ferrero et al. 2007; (12) Levan et al. 2008; (13) Berger et al. 2007; (14) Soderberg et al. 2006; (15) Levan et al. 2006; (16) Price et al. 2006b; (17) Jin et al. 2015; (18) Stratta et al. 2007; (19) Malesani et al. 2007b; (20) Perley et al. 2007c; (21) Nysewander et al. 2007; (22) Piranomonte et al. 2008; (23) Covino et al. 2007; (24) Levan et al. 2007; (25) Perley et al. 2007b; (26) Berger et al. 2009; (27) Nicuesa Guelbenzu et al. 2012; (28) Perley et al. 2007a; (29) Berger & Challis 2007; (30) Perley et al. 2009; (31) Rowlinson et al. 2010b; (32) Tunnicliffe et al. 2014; (33) Rowlinson et al. 2010a; (34) Galeev et al. 2009; (35) Perley et al. 2012; (36) Fong et al. 2015; (37) Fong et al. 2013; (38) Fong et al. 2012b; (39) Sakamoto et al. 2013; (40) Margutti et al. 2012; (41) Rossi et al. 2012; (42) Fong et al. 2012a; (43) Xu et al. 2013; (44) D'Avanzo et al. 2013; (45) Cenko & Cucchiara 2013; (46) Berger et al. 2013; (47) Tanvir et al. 2013a; (48) Cenko et al. 2013; (49) Tanvir et al. 2013b; (50) Butler et al. 2013; (51) Littlejohns et al. 2013; (52) Pandey et al. 2019; (53) Gorosabel et al. 2014; (54) Minowa et al. 2014; (55) Butler et al. 2014; (56) Fong et al. 2016; (57) Wiersema et al. 2015; (58) Littlejohns et al. 2015; (59) Knust et al. 2017; (60) Jin et al. 2018; (61) Knust et al. 2015; (62) Troja et al. 2016a; (63) Graham et al. 2016; (64) Malesani et al. 2016; (65) Yates et al. 2016; (66) Cenko & Troja 2016; (67) Cucchiara & Levan 2016; (68) O'Connor et al. 2021; (69) Lamb et al. 2019; (70) Troja et al. 2019; (71) Chen et al. 2016; (72) Nugent et al. 2020; (73) Cano et al. 2017; (74) Rouco Escorial et al. 2021; (75) Malesani et al. 2018; (76) Higgins et al. 2018; (77) Paterson et al. 2020; (78) Tanvir & Fong 2018; (79) De 2018; (80) Izzo et al. 2019; (81) Butler et al. 2019; (82) Dichiara & Troja 2019; (83) Fong et al. 2021; (84) Rossi et al. 2020a. **Redshift References**: Bloom et al. (2006), Berger et al. (2005), Prochaska et al. (2006), Soderberg et al. (2006), Bloom et al. (2007), Price et al. (2006a), Stratta et al. (2007), Berger (2006), Cenko et al. (2008), Berger et al. (2009), Nugent et al. (2020), Berger (2010), Rowlinson et al. (2010b), Rowlinson et al. (2010a), Perley et al. (2012), Fong et al. (2013), Selsing et al. (2018), Wiersema et al. (2013), Chornock et al. (2013), Troja et al. (2016b), Chornock et al. (2014), Chornock & Fong (2015), Selsing et al. (2019), Fong et al. (2015), Fong et al. (2016), Cucchiara & Levan (2016), Lamb et al. (2019), Troja et al. (2019), Nugent et al. (2020), Izzo et al. (2017), Rouco Escorial et al. (2021), This work (GRB 180805B), Paterson et al. (2020), Fong et al. (2021), de Ugarte Postigo et al. (2020).
(This table is available in machine-readable form.)
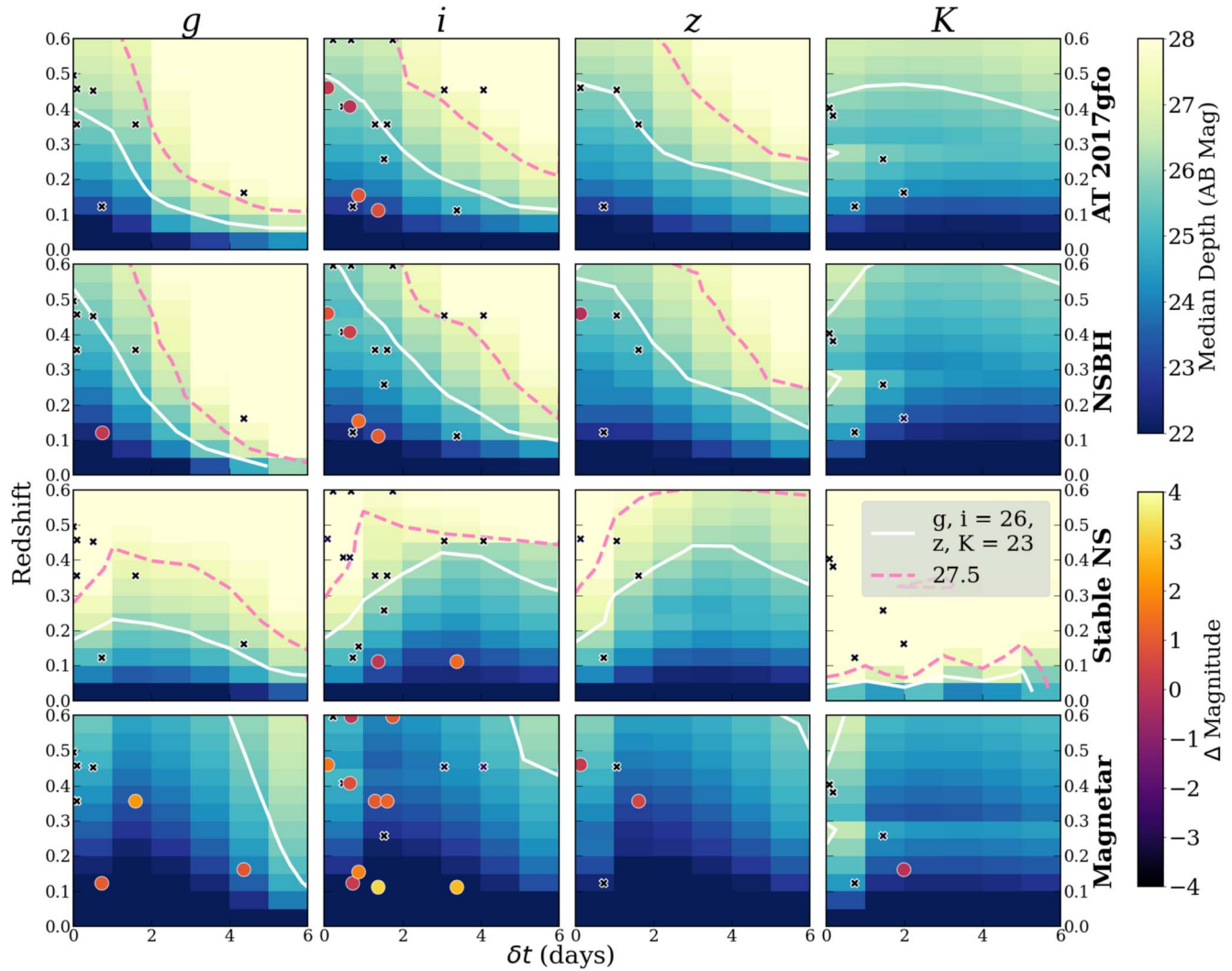
Figure A1. The same analysis as Figure 6 and described in Section 5.3, but shown in the observed g, i, z, and K bands. As also demonstrated by Figure 6, the optical bands are generally more populated with observations of low-redshift bursts than the NIR.

ORCID iDs

J. C. Rastinejad https://orcid.org/0000-0002-9267-6213
W. Fong https://orcid.org/0000-0002-7374-935X
C. D. Kilpatrick https://orcid.org/0000-0002-5740-7747
K. Paterson https://orcid.org/0000-0001-8340-3486
N. R. Tanvir https://orcid.org/0000-0003-3274-6336
A. J. Levan https://orcid.org/0000-0001-7821-9369
B. D. Metzger https://orcid.org/0000-0002-4670-7509
E. Berger https://orcid.org/0000-0002-9392-9681
R. Chornock https://orcid.org/0000-0002-7706-5668
B. E. Cobb https://orcid.org/0000-0002-9118-9448
T. Laskar https://orcid.org/0000-0003-1792-2338
P. Milne https://orcid.org/0000-0002-0370-157X
A. E. Nugent https://orcid.org/0000-0002-2028-9329
N. Smith https://orcid.org/0000-0001-5510-2424

References

Abbott, B. P., Abbott, R., Abbott, T. D., et al. 2017a, ApJL, 848, L12
Abbott, B. P., Abbott, R., Abbott, T. D., et al. 2017b, ApJL, 848, L13
Abbott, B. P., Abbott, R., Abbott, T. D., et al. 2017c, PhRvL, 119, 161101
Abbott, B. P., Abbott, R., Abbott, T. D., et al. 2020a, ApJL, 892, L3
Abbott, R., Abbott, T. D., Abraham, S., et al. 2020b, ApJL, 896, L44

Abbott, R., Abbott, T. D., Abraham, S., et al. 2021, PhRvX, 11, 021053
Ackley, K., Amati, L., Barbieri, C., et al. 2020, A&A, 643, A113
Alam, S., Albareti, F. D., Allende Prieto, C., et al. 2015, ApJS, 219, 12
Anand, S., Andreoni, I., Goldstein, D. A., et al. 2021, NatAs, 5, 46
Andreoni, I., Ackley, K., Cooke, J., et al. 2017, PASA, 34, e069
Andreoni, I., Goldstein, D. A., Kasliwal, M. M., et al. 2020, ApJ, 890, 131
Arcavi, I., Hosseinzadeh, G., Howell, D. A., et al. 2017, Natur, 551, 64
Arnett, W. D. 1982, ApJ, 253, 785
Ascenzi, S., Coughlin, M. W., Dietrich, T., et al. 2019, MNRAS, 486, 672
Astropy Collaboration, Price-Whelan, A. M., Sipőcz, B. M., et al. 2018, AJ,
    156, 123
Astropy Collaboration, Robitaille, T. P., Tollerud, E. J., et al. 2013, A&A,
    558, A33
Banerjee, S., Tanaka, M., Kawaguchi, K., Kato, D., & Gaigalas, G. 2020, ApJ,
    901, 29
Barbieri, C., Salafia, O. S., Colpi, M., Ghirlanda, G., & Perego, A. 2020,
    arXiv:2002.09395
Barnes, J., & Kasen, D. 2013, ApJ, 775, 18
Barnes, J., Kasen, D., Wu, M.-R., & Martínez-Pinedo, G. 2016, ApJ, 829, 110
Becker, A. 2015, HOTPANTS: High Order Transform of PSF ANd Template
    Subtraction, Astrophysics Source Code Library, ascl:1504.004
Bennett, C. L., Larson, D., Weiland, J. L., & Hinshaw, G. 2014, ApJ, 794, 135
Berger, E. 2006, GCN, 5965, 1
Berger, E. 2007, ApJ, 670, 1254
Berger, E. 2010, ApJ, 722, 1946
Berger, E. 2014, ARA&A, 52, 43
Berger, E., Cenko, S. B., Fox, D. B., & Cucchiara, A. 2009, ApJ, 704, 877
Berger, E., & Challis, P. 2007, GCN, 7085, 1

Berger, E., Fong, W., & Chornock, R. 2013, ApJL, 774, L23
Berger, E., Fox, D. B., Price, P. A., et al. 2007, ApJ, 664, 1000
Berger, E., Price, P. A., Cenko, S. B., et al. 2005, Natur, 438, 988
Beroiz, M., Cabral, J. B., & Sanchez, B. 2020, A&C, 32, 100384
Bloom, J. S., Kulkarni, S. R., & Djorgovski, S. G. 2002, AJ, 123, 1111
Bloom, J. S., Perley, D. A., Chen, H. W., et al. 2007, ApJ, 654, 878
Bloom, J. S., Prochaska, J. X., Pooley, D., et al. 2006, ApJ, 638, 354
Broekgaarden, F. S., Berger, E., Neijssel, C. J., et al. 2021, arXiv:2103.02608
Bucciantini, N., Metzger, B. D., Thompson, T. A., & Quataert, E. 2012, MNRAS, 419, 1537
Butler, N., Watson, A. M., Kutyrev, A., et al. 2013, GCN, 15226, 1
Butler, N., Watson, A. M., Kutyrev, A., et al. 2014, GCN, 16297, 1
Butler, N., Watson, A. M., Kutyrev, A., et al. 2019, GCN, 26121, 1
Cano, Z., Heintz, K. E., Malesani, D., & Tronsgaard, R. 2017, GCN, 20549, 1
Cantiello, M., Jensen, J. B., Blakeslee, J. P., et al. 2018, ApJL, 854, L31
Castro-Tirado, A. J., de Ugarte Postigo, A., Gorosabel, J., et al. 2005, A&A, 439, L15
Castro-Tirado, A. J., Sanchez-Ramirez, R., Lombardi, G., & Rivero, M. A. 2015, GCN, 17758, 1
Cenko, S. B., Berger, E., Nakar, E., et al. 2008, arXiv:0802.0874
Cenko, S. B., & Cucchiara, A. 2013, GCN, 14670, 1
Cenko, S. B., Perley, D. A., Cucchiara, A., Fong, W., & Levan, A. J. 2013, GCN, 15121, 1
Cenko, S. B., Soifer, B. T., Bian, C., et al. 2005, GCN, 3409, 1
Cenko, S. B., & Troja, E. 2016, GCN, 19497, 1
Chambers, K. C., Magnier, E. A., Metcalfe, N., et al. 2016, arXiv:1612.05560
Chen, T. W., Klose, S., Guelbenzu, A. N., et al. 2016, GCN, 19975, 1
Chornock, R., Berger, E., Kasen, D., et al. 2017, ApJL, 848, L19
Chornock, R., & Fong, W. 2015, GCN, 17358, 1
Chornock, R., Fong, W., & Fox, D. B. 2013, GCN, 17177, 1
Chornock, R., Lunnan, R., & Berger, E. 2013, GCN, 15307, 1
Christie, I. M., Lalakos, A., Tchekhovskoy, A., et al. 2019, MNRAS, 490, 4811
Church, R. P., Levan, A. J., Davies, M. B., & Tanvir, N. 2011, MNRAS, 413, 2004
Collaboration, F.-L. 2017, Fermi-LAT observations of the LIGO/Virgo event GW170817, arXiv:1710.05450
Coughlin, M. W., Ahumada, T., Anand, S., et al. 2019, ApJL, 885, L19
Coughlin, M. W., Dietrich, T., Antier, S., et al. 2020, MNRAS, 492, 863
Coughlin, M. W., Dietrich, T., Doctor, Z., et al. 2018, MNRAS, 480, 3871
Coulter, D. A., Foley, R. J., Kilpatrick, C. D., et al. 2017, Sci, 358, 1556
Covino, S., Malesani, D., Israel, G. L., et al. 2006, A&A, 447, L5
Covino, S., Piranomonte, S., D'Avanzo, P., et al. 2007, GCN, 6635, 1
Cowperthwaite, P. S., Berger, E., Villar, V. A., et al. 2017, ApJL, 848, L17
Cucchiara, A., & Levan, A. J. 2016, GCN, 19565, 1
D'Avanzo, P., Covino, S., Melandri, A., Padilla Torres, C. P., & Andreuzzi, G. 2013, GCN, 14307, 1
D'Avanzo, P., Malesani, D., Covino, S., et al. 2009, A&A, 498, 711
De, K. 2018, GCN, 23462, 1
Della Valle, M., Chincarini, G., Panagia, N., et al. 2006, Natur, 444, 1050
Dessart, L., Ott, C. D., Burrows, A., Rosswog, S., & Livne, E. 2009, ApJ, 690, 1681
de Ugarte Postigo, A., Kann, D. A., Izzo, L., et al. 2020, GCN, 29132, 1
Díaz, M. C., Macri, L. M., Garcia Lambas, D., et al. 2017, ApJL, 848, L29
Dichiara, S., & Troja, E. 2019, GCN, 26147, 1
Drout, M. R., Piro, A. L., Shappee, B. J., et al. 2017, Sci, 358, 1570
Evans, P. A., Beardmore, A. P., Page, K. L., et al. 2009, MNRAS, 397, 1177
Evans, P. A., Cenko, S. B., Kennea, J. A., et al. 2017, Sci, 358, 1565
Fahlman, S., & Fernández, R. 2018, ApJL, 869, L3
Fernández, R., & Metzger, B. D. 2016, ARNPS, 66, 23
Fernández, R., Tchekhovskoy, A., Quataert, E., Foucart, F., & Kasen, D. 2019, MNRAS, 482, 3373
Ferrero, P., Sanchez, S. F., Kann, D. A., et al. 2007, AJ, 134, 2118
Foley, R. J., Coulter, D. A., Kilpatrick, C. D., et al. 2020, MNRAS, 494, 190
Fong, W., & Berger, E. 2013, ApJ, 776, 18
Fong, W., Berger, E., Blanchard, P. K., et al. 2017, ApJL, 848, L23
Fong, W., Berger, E., Chornock, R., et al. 2013, ApJ, 769, 56
Fong, W., Berger, E., Kelson, D., & Williams, R. 2012a, GCN, 13700, 1
Fong, W., Berger, E., Margutti, R., et al. 2012b, ApJ, 756, 189
Fong, W., Berger, E., Margutti, R., & Zauderer, B. A. 2015, ApJ, 815, 102
Fong, W., Laskar, T., Rastinejad, J., et al. 2021, ApJ, 906, 127
Fong, W., Margutti, R., Chornock, R., et al. 2016, ApJ, 833, 151
Foucart, F., Deaton, M. B., Duez, M. D., et al. 2013, PhRvD, 87, 084006
Foucart, F., Hinderer, T., & Nissanke, S. 2018, PhRvD, 98, 081501
Fox, D. B., Frail, D. A., Price, P. A., et al. 2005, Natur, 437, 845
Galeev, A., Bikmaev, I., Sakhibullin, N., et al. 2009, GCN, 9549, 1
Gall, C., Hjorth, J., Rosswog, S., Tanvir, N. R., & Levan, A. J. 2017, ApJ, 849, L19
Gal-Yam, A., Fox, D. B., Price, P. A., et al. 2006, Natur, 444, 1053
Gao, H., Zhang, B., Lü, H.-J., & Li, Y. 2017, ApJ, 837, 50
Gehrels, N., Chincarini, G., Giommi, P., et al. 2004, ApJ, 611, 1005
Gehrels, N., Norris, J. P., Barthelmy, S. D., et al. 2006, Natur, 444, 1044
Ghirlanda, G., Salafia, O. S., Paragi, Z., et al. 2019, Sci, 363, 968
Goldstein, A., Veres, P., Burns, E., et al. 2017, ApJ, 848, L14
Gomez, S., Hosseinzadeh, G., Cowperthwaite, P. S., et al. 2019, ApJL, 884, L55
Gompertz, B. P., Cutter, R., Steeghs, D., et al. 2020a, MNRAS, 497, 726
Gompertz, B. P., Levan, A. J., Tanvir, N. R., et al. 2018, ApJ, 860, 62
Gompertz, B. P., Levan, A. J., & Tanvir, N. R. 2020b, ApJ, 895, 58
Gorosabel, J., Xu, D., de Ugarte Postigo, A., et al. 2014, GCN, 16290, 1
Graham, J., Bolmer, J., Wiseman, P., & Greiner, J. 2016, GCN, 19144, 1
Harris, C. R., Millman, K. J., van der Walt, S. J., et al. 2020, Natur, 585, 357
Hempel, M., & Schaffner-Bielich, J. 2010, NuPhA, 837, 210
Higgins, A., Wiersema, K., & Malesani, D. B. 2018, GCN, 23090, 1
Hjorth, J., Sollerman, J., Gorosabel, J., et al. 2005a, ApJL, 630, L117
Hjorth, J., Watson, D., Fynbo, J. P. U., et al. 2005b, Natur, 437, 859
Hosseinzadeh, G., Cowperthwaite, P. S., Gomez, S., et al. 2019, ApJL, 880, L4
Hotokezaka, K., Kyutoku, K., Tanaka, M., et al. 2013, ApJL, 778, L16
Hotokezaka, K., Nakar, E., Gottlieb, O., et al. 2019, NatAs, 3, 940
Hu, L., Wu, X., Andreoni, I., et al. 2017, Science Bulletin, 62, 1433
Izzo, L., Cano, Z., de Ugarte Postigo, A., et al. 2017, GCN, 21059, 1
Izzo, L., Malesani, D. B., Xu, D., & Jannsen, N. 2019, GCN, 24265, 1
Jespersen, C. K., Severin, J. B., Steinhardt, C. L., et al. 2020, ApJL, 896, L20
Jin, Z.-P., Covino, S., Liao, N.-H., et al. 2020, NatAs, 4, 77
Jin, Z.-P., Hotokezaka, K., Li, X., et al. 2016, NatCo, 7, 12898
Jin, Z.-P., Li, X., Cano, Z., et al. 2015, ApJL, 811, L22
Jin, Z.-P., Li, X., Wang, H., et al. 2018, ApJ, 857, 128
Just, O., Bauswein, A., Ardevol Pulpillo, R., Goriely, S., & Janka, H. T. 2015, MNRAS, 448, 541
Kasen, D., Badnell, N. R., & Barnes, J. 2013, ApJ, 774, 25
Kasen, D., Fernández, R., & Metzger, B. D. 2015, MNRAS, 450, 1777
Kasen, D., Metzger, B., Barnes, J., Quataert, E., & Ramirez-Ruiz, E. 2017, Natur, 551, 80
Kasen, D., Thomas, R. C., & Nugent, P. 2006, ApJ, 651, 366
Kasliwal, M. M., Korobkin, O., Lau, R. M., Wollaeger, R., & Fryer, C. L. 2017b, ApJ, 843, L34
Kasliwal, M. M., Nakar, E., Singer, L. P., et al. 2017a, Sci, 358, 1559
Kawaguchi, K., Kyutoku, K., Shibata, M., & Tanaka, M. 2016, ApJ, 825, 52
Kawaguchi, K., Shibata, M., & Tanaka, M. 2020a, ApJ, 889, 171
Kawaguchi, K., Shibata, M., & Tanaka, M. 2020b, ApJ, 893, 153
Kilpatrick, C. D., Foley, R. J., Kasen, D., et al. 2017, Sci, 358, 1583
Kim, C., Perera, B. B. P., & McLaughlin, M. A. 2015, MNRAS, 448, 928
Knust, F., Greiner, J., van Eerten, H. J., et al. 2017, A&A, 607, A84
Knust, F., Klose, S., & Greiner, J. 2015, GCN, 18219, 1
Kouveliotou, C., Meegan, C. A., Fishman, G. J., et al. 1993, ApJL, 413, L101
Kyutoku, K., Fujibayashi, S., Hayashi, K., et al. 2020, ApJL, 890, L4
Kyutoku, K., Ioka, K., Okawa, H., Shibata, M., & Taniguchi, K. 2015, PhRvD, 92, 044028
Lamb, G. P., Tanvir, N. R., Levan, A. J., et al. 2019, ApJ, 883, 48
Lang, D., Hogg, D. W., Mierle, K., Blanton, M., & Roweis, S. 2010, AJ, 139, 1782
Levan, A. J., Tanvir, N. R., & Davis, C. 2007, GCN, 6662, 1
Levan, A. J., Tanvir, N. R., Fruchter, A. S., et al. 2006, ApJL, 648, L9
Levan, A. J., Tanvir, N. R., Jakobsson, P., et al. 2008, MNRAS, 384, 541
Li, L.-X., & Paczyński, B. 1998, ApJL, 507, L59
Lien, A., Sakamoto, T., Barthelmy, S. D., et al. 2016, ApJ, 829, 7
Lippuner, J., Fernández, R., Roberts, L. F., et al. 2017, MNRAS, 472, 904
Lipunov, V. M., Gorbovskoy, E., Kornilov, V. G., et al. 2017, ApJL, 850, L1
Littlejohns, O., Butler, N., Watson, A. M., et al. 2013, GCN, 15312, 1
Littlejohns, O., Butler, N., Watson, A. M., et al. 2013, GCN, 17754, 1
Malesani, D., Covino, S., D'Avanzo, P., et al. 2007a, A&A, 473, 77
Malesani, D., Uthas, H., Thoene, C. C., et al. 2007b, GCN, 6254, 1
Malesani, D., Xu, D., & Kuutma, T. 2016, GCN, 19300, 1
Malesani, D. B., Pugliese, G., D'Avanzo, P., Tanvir, N. R., & Wiersema, K. 2018, GCN, 23086, 1
Margalit, B., & Metzger, B. D. 2019, ApJL, 880, L15
Margutti, R., Berger, E., Fong, W., et al. 2012, ApJ, 756, 63
Margutti, R., & Chornock, R. 2020, arXiv:2012.04810
McBrien, O. R., Smartt, S. J., Huber, M. E., et al. 2020, MNRAS, 500, 4213
McCully, C., Hiramatsu, D., Howell, D. A., et al. 2017, ApJL, 848, L32
Mereghetti, S., Götz, D., Borkowski, J., Walter, R., & Pedersen, H. 2003, A&A, 411, L291

Metzger, B. D. 2017, arXiv:1710.05931

Metzger, B. D. 2019, LRR, 23, 1

Metzger, B. D., Bauswein, A., Goriely, S., & Kasen, D. 2015, MNRAS, 446, 1115

Metzger, B. D., & Fernández, R. 2014, MNRAS, 441, 3444

Metzger, B. D., Martínez-Pinedo, G., Darbha, S., et al. 2010, MNRAS, 406, 2650

Metzger, B. D., & Piro, A. L. 2014, MNRAS, 439, 3916

Metzger, B. D., Piro, A. L., & Quataert, E. 2008, MNRAS, 390, 781

Metzger, B. D., Piro, A. L., & Quataert, E. 2009, MNRAS, 396, 304

Metzger, B. D., Thompson, T. A., & Quataert, E. 2018, ApJ, 856, 101

Minowa, Y., Pyo, T. S., Kim, J. H., & Kawai, N. 2014, GCN, 16296, 1

Monet, D. G., Levine, S. E., Canzian, B., et al. 2003, AJ, 125, 984

Mooley, K. P., Deller, A. T., Gottlieb, O., et al. 2018, Natur, 561, 355

Morgan, R., Soares-Santos, M., Annis, J., et al. 2020, ApJ, 901, 83

Nicholl, M., Berger, E., Kasen, D., et al. 2017, ApJL, 848, L18

Nicuesa Guelbenzu, A., Klose, S., Greiner, J., et al. 2012, A&A, 548, A101

Norris, J. P., Cline, T. L., Desai, U. D., & Teegarden, B. J. 1984, Natur, 308, 434

Nugent, A. E., Fong, W., Dong, Y., et al. 2020, ApJ, 904, 52

Nysewander, M., Fruchter, A., & Graham, J. 2007, GCN, 6604, 1

O'Connor, B., Troja, E., Dichiara, S., et al. 2021, MNRAS, 502, 1279

Pandey, S. B., Hu, Y., Castro-Tirado, A. J., et al. 2019, MNRAS, 485, 5294

Parsons, A. M., Cummings, J. R., Gehrels, N., et al. 2006, GCN, 5252, 1

Paterson, K., Fong, W., Nugent, A., et al. 2020, ApJL, 898, L32

Paterson, K., Lundquist, M. J., Rastinejad, J. C., et al. 2021, ApJ, 912, 128

Perego, A., Radice, D., & Bernuzzi, S. 2017, ApJL, 850, L37

Perego, A., Rosswog, S., Cabezón, R. M., et al. 2014, MNRAS, 443, 3134

Perley, D. A., Bloom, J. S., Modjaz, M., Poznanski, D., & Thoene, C. C. 2007a, GCN, 7140, 1

Perley, D. A., Bloom, J. S., Thoene, C., & Butler, N. R. 2007b, GCN, 6652, 1

Perley, D. A., Metzger, B. D., Granot, J., et al. 2009, ApJ, 696, 1871

Perley, D. A., Modjaz, M., Morgan, A. N., et al. 2012, ApJ, 758, 122

Perley, D. A., Thoene, C. C., & Bloom, J. S. 2007c, GCN, 6774, 1

Pian, E., D'Avanzo, P., Benetti, S., et al. 2017, Natur, 551, 67

Piranomonte, S., D'Avanzo, P., Covino, S., et al. 2008, A&A, 491, 183

Piro, A. L., & Kollmeier, J. A. 2018, ApJ, 855, 103

Pozanenko, A. S., Barkov, M. V., Minaev, P. Y., et al. 2018, ApJL, 852, L30

Price, P. A., Berger, E., & Fox, D. B. 2006a, GCN, 5275, 1

Price, P. A., Berger, E., Fox, D. B., Cenko, S. B., & Rau, A. 2006b, GCN, 5077, 1

Prochaska, J. X., Bloom, J. S., Chen, H. W., et al. 2006, ApJ, 642, 989

Radice, D., Perego, A., Bernuzzi, S., & Zhang, B. 2018, MNRAS, 481, 3670

Rossi, A., D'Avanzo, P. & CIBO Collaboration 2020a, GCN, 28034, 1

Rossi, A., Nardini, M., Klose, S., & Greiner, J. 2012, GCN, 13335, 1

Rossi, A., Stratta, G., Maiorano, E., et al. 2020b, MNRAS, 493, 3379

Rosswog, S. 2005, ApJ, 634, 1202

Rosswog, S., Feindt, U., Korobkin, O., et al. 2017, CQGra, 34, 104001

Rosswog, S., Korobkin, O., Arcones, A., Thielemann, F. K., & Piran, T. 2014, MNRAS, 439, 744

Rosswog, S., Sollerman, J., Feindt, U., et al. 2018, A&A, 615, A132

Rouco Escorial, A., Fong, W.-F., Veres, P., et al. 2021, ApJ, 912, 95

Rowlinson, A., O'Brien, P. T., Tanvir, N. R., et al. 2010a, MNRAS, 409, 531

Rowlinson, A., Wiersema, K., Levan, A. J., et al. 2010b, MNRAS, 408, 383

Sakamoto, T., Troja, E., Aoki, K., et al. 2013, ApJ, 766, 41

Sari, R., Piran, T., & Narayan, R. 1998, ApJL, 497, L17

Savchenko, V., Ferrigno, C., Kuulkers, E., et al. 2017, ApJL, 848, L15

Schroeder, G., Margalit, B., Fong, W.-f., et al. 2020, ApJ, 902, 82

Scolnic, D., Kessler, R., Brout, D., et al. 2018, ApJL, 852, L3

Sekiguchi, Y., Kiuchi, K., Kyotoku, K., & Shibata, M. 2015, PhRvD, 91, 064059

Selsing, J., Krühler, T., Malesani, D., et al. 2018, A&A, 616, A48

Selsing, J., Malesani, D., Goldoni, P., et al. 2019, A&A, 623, A92

Shappee, B. J., Simon, J. D., Drout, M. R., et al. 2017, Sci, 358, 1574

Shen, S., Cooke, R. J., Ramirez-Ruiz, E., et al. 2015, ApJ, 807, 115

Shibata, M., & Hotokezaka, K. 2019, ARNPS, 69, 41

Siegel, D. M. 2019, EPJA, 55, 203

Siegel, D. M., Barnes, J., & Metzger, B. D. 2019, Natur, 569, 241

Skrutskie, M. F., Cutri, R. M., Stiening, R., et al. 2006, AJ, 131, 1163

Smartt, S. J., Chen, T. W., Jerkstrand, A., et al. 2017, Natur, 551, 75

Soares-Santos, M., Holz, D. E., Annis, J., et al. 2017, ApJL, 848, L16

Soderberg, A. M., Berger, E., Kasliwal, M., et al. 2006, ApJ, 650, 261

Stratta, G., D'Avanzo, P., Piranomonte, S., et al. 2007, A&A, 474, 827

STScI Development Team 2013, Pysynphot: Synthetic Photometry Software Package, Astrophysics Source Code Library, ascl:1303.023

Tanaka, M., Kato, D., Gaigalas, G., & Kawaguchi, K. 2020, MNRAS, 496, 1369

Tanvir, N. R., & Fong, W. 2018, GCN, 23458, 1

Tanvir, N. R., Levan, A. J., Fruchter, A. S., et al. 2013a, Natur, 500, 547

Tanvir, N. R., Levan, A. J., González-Fernández, C., et al. 2017, ApJL, 848, L27

Tanvir, N. R., Wiersema, K., & Levan, A. J. 2013b, GCN, 15224, 1

Tody, D. 1986, Proc. SPIE, 627, 733

Tody, D. 1993, in ASP Conf. Ser. 52, Astronomical Data Analysis Software and Systems II, ed. R. J. Hanisch, R. J. V. Brissenden, & J. Barnes (San Francisco, CA: ASP), 173

Troja, E., Butler, N., Watson, A. M., et al. 2016a, GCN, 19146, 1

Troja, E., Castro-Tirado, A. J., Becerra González, J., et al. 2019, MNRAS, 489, 2104

Troja, E., Piro, L., van Eerten, H., et al. 2017, Natur, 551, 71

Troja, E., Ryan, G., Piro, L., et al. 2018, NatCo, 9, 4089

Troja, E., Sakamoto, T., Cenko, S. B., et al. 2016b, ApJ, 827, 102

Tunnicliffe, R. L., Levan, A. J., Tanvir, N. R., et al. 2014, MNRAS, 437, 1495

Typel, S., Röpke, G., Klähn, T., Blaschke, D., & Wolter, H. H. 2010, PhRvC, 81, 015803

Utsumi, Y., Tanaka, M., Tominaga, N., et al. 2017, PASJ, 69, 101

Valenti, S., Sand, D. J., Yang, S., et al. 2017, ApJL, 848, L24

Vieira, N., Ruan, J. J., Haggard, D., et al. 2020, ApJ, 895, 96

Villar, V. A., Guillochon, J., Berger, E., et al. 2017, ApJL, 851, L21

Wanajo, S., Sekiguchi, Y., Nishimura, N., et al. 2014, ApJL, 789, L39

Wiersema, K., Levan, A., Cenko, S. B., & Tanvir, N. 2013, GCN, 15178, 1

Wiersema, K., Levan, A., Tanvir, N., MacLeod, C., & Riddick, F. 2015, GCN, 17747, 1

Xu, D., Schulze, S., Tanvir, N. R., Dahle, H., & Fynbo, J. P. U. 2013, GCN, 14301, 1

Yamaoka, K., Sugita, S., Ohno, M., et al. 2006, Proc. SPIE, 6266, 626643

Yang, B., Jin, Z.-P., Li, X., et al. 2015, NatCo, 6, 7323

Yates, R., Chen, T. W., & Greiner, J. 2016, GCN, 19292, 1